國立臺灣大學理學院物理學研究所

碩士論文

Department of Physics

College of Science

National Taiwan University

Master Thesis

單軸應力對少數層硒化銦角分析二倍頻的影響

Effect of Uniaxial Strain on Angle-Resolved Second Harmonic Generation from Few-Layer InSe

李資怡

Zi-Yi Li

指導教授： 陳永芳 博士

Advisor: Yang-Fang Chen, Ph.D.

共同指導教授：林宮玄 博士

Co-Advisor: Kung-Hsuan Lin, Ph.D.

中華民國 112 年 7 月

July, 2023

doi:10.6342/NTU202301960

國立臺灣大學碩士學位論文
口試委員會審定書
MASTER'S THESIS ACCEPTANCE CERTIFICATE
NATIONAL TAIWAN UNIVERSITY

單軸應力對少數層硒化銦角分析二倍頻的影響

Effect of Uniaxial Strain on Angle-Resolved Second Harmonic Generation from Few-Layer InSe

本論文係 李資怡 (姓名) R10222010 (學號) 在國立臺灣大學 物理所 (系/所/學位學程)完成之碩士學位論文，於民國 112 年 7 月 4 日承下列考試委員審查通過及口試及格，特此證明。

The undersigned, appointed by the Department / Institute of physics on 4th July 2023 have examined a Master's thesis entitled above presented by Zi-Yi Li (R10222010) candidate and hereby certify that it is worthy of acceptance.

口試委員 Oral examination committee:

(指導教授 Advisor)		

系主任/所長 Director: 理學院物理學系系主任張寶棣

Acknowledgements

I would like to express my gratitude to my supervisor, Dr. Kung-Hsuan Lin for his guidance and support throughout this research project. He has provided me with valuable insights and advice on various aspects of the project, which have been invaluable in helping me to understand the project better and to make informed decisions.

I would also like to acknowledge the support of the lab member, Hao-Yu Cheng, who provided the assistance and the guidance for the optical experiments. Furthermore, I would like to thank Dr. Chi-Cheng Lee for providing the program of first-principles calculation and the lab members, Sheng-Hsun Kung and Redhwan, for teaching me the details of the calculation processes. Without their guidance and support, it would have been impossible to complete this project to the best of my abilities.

Besides the assistances from the group members, this project also obtained support from the organizations. I would like to acknowledge National Science and Technology Council (NSTC) for providing the financial support for this project, and the Institute of Physics, Academia Sinica for providing the shared facility, which allowed us to access more resources to complete this work.

Finally, I would like to thank the Lab group members and the committee of the defense for their suggestions for the thesis. Above all, thanks for those supports, guidance, suggestions from people related to this project. They have all played a significant role in making this project a success and I am grateful for their contributions.

doi:10.6342/NTU202301960

中文摘要

硒化銦晶體是一種新興的凡德瓦材料，具有良好的電性與光電特性，並且已被應用於製成元件。此種層狀堆疊的材料在少數層時具有良好的彈性，使其具有被應用在彈性元件上的潛力，探討應力如何改變硒化銦的光電特性便成為一個重要的議題。然而，在進行應力與硒化銦光電特性的探討前，需要得知如何量測硒化銦之應力大小，本次研究目的便是藉由探討硒化銦二倍頻與其所受應力大小的關係，以期使二倍頻技術應用於測量硒化銦所受應力。

近年來有許多技術能直接或間接地測量材料所受之應力大小，而利用二倍頻量測也是其中之一。由於二倍頻對於材料的結構息息相關，透過測量材料不同角度的二倍頻訊號能解析材料的結構，也因此當材料受應力而產生結構改變時，會使二倍頻訊號受影響，若測量不同應力下的角分析二倍頻，能得出材料所受的應力方向以及大小。

本篇論文探討硒化銦少數層受單軸應力時，其角分析二倍頻的變化。在實驗方面，我們透過測量拉曼光譜確認晶體為硒化銦，並以光致螢光光譜得知其能隙。由於層狀結構的硒化銦晶體可以不同的堆疊方式構成，我們利用斜向入射二倍頻的技術得知硒化銦的相位為γ，並以剝離的製程方式得到少數層硒化銦，將其放置於透明且具彈性的基板上。利用自製的應力裝置擠壓基板的左右兩側，使其形變，施加單軸壓縮應力於少數層硒化銦，並利用脈衝雷射激發硒化銦產生二倍頻訊號。我們得到角分析二倍頻的方式是旋轉樣品本身，在不同的選轉角度下測量其二倍頻訊號。從實驗結果得知硒化銦的角分析二倍頻訊號隨壓縮應力增加而減小。

理論計算方面，我們利用第一原理進行硒化銦的電子結構計算，並更進一步得到不同應力下硒化銦的二階極化率，藉由數學計算二倍頻與角度的關係，結合第一原理的計算結果與數學公式，得出理論上硒化銦受單軸壓縮應變時，其角分析二倍頻的訊號亦會遞減。

儘管實驗和理論結果都顯示了二倍頻隨應力增加而減小的現象，我們使用基

doi:10.6342/NTU202301960

於第一原理結果的模型來擬合實驗數據時發現仍存在差異。我們利用計算相關係數的方式得知理論模型與實驗數據的相關性。結果顯示，隨著應力越大，相關係數的值變小，可知由第一原理計算的變化較實際值小，因而在應力較大時與實驗值的結果較不吻合。然而，在應力變化項的部分增加一修正項時，實驗數據與模型能在各個應力下得到良好的擬合結果。

關鍵字: 硒化銦，角分析二倍頻，應力，第一原理計算，非線性光學

doi:10.6342/NTU202301960

Abstract

Indium selenide (InSe) is an emerging van der Waals material. It exhibits well electronic and optoelectronic properties for devices. This layered material possesses well deformability when it consists of few-layers such that it applicable to flexible devices. Therefore, how strain influences InSe becomes an important issue. Recently, many techniques have been developed to measure the strain on materials, and one of them is second harmonic generation (SHG). Owing to the structure-sensitive properties, the angle-resolved SHG pattern is able to reflect the structure of the material. While the structure of the material is deformed due to the strain, the angle-resolved SHG pattern will also vary accordingly. Therefore, the angle-resolved SHG pattern can be used to measure strain on the material.

In the thesis, we systematically investigated the effect of strain on angle-resolved SHG from few-layers InSe. In the experiment, we used oblique incident SHG technique to identify the phase of the InSe crystal. The few-layers InSe sample was prepared by mechanical exfoliation and placed on a flexible and transparent substrate. With the self-designed strain device, we were able to apply the strain on the sample by pushing the substrate from the two sides. To measure the SHG from InSe, we used pulse laser to induce the nonlinear effect from InSe. The way we obtain angle-resolved SHG is by rotating the sample itself and measuring its SHG at different rotation angles. The results

doi:10.6342/NTU202301960

show the SHG intensity decreases while the compressive strain level increases.

For the theoretical approach, we used first-principles method based on density functional theory (DFT) and generalized gradient approximation (GGA) to calculate the electronic structure and the second-order susceptibility of InSe. Integrating with the mathematical description and the first-principles results, we obtained the relation between compressive strain and the angle-resolved SHG, which also reveals decreased intensity with increasing strain level.

Despite the fact that the experimental and theoretical results exhibit similar strain effects, there is a discrepancy between them as the experimental data was fitted using a model based on the first-principles results. To quantitatively understand this difference, we calculated the coefficient of determination (r-squared) values of the fitting results for each strain case. The results showed that the r-squared value decreased with increasing strain, indicating that the first-principles method underestimated the strain effect. However, by incorporating a correction term to modify the fitting model, the first-principles results were able to agree well with the experimental results.

Keywords: InSe, Angle-resolved second harmonic generation, Strain, First-principles calculation, Nonlinear optics

doi:10.6342/NTU202301960

Contents

doi:10.6342/NTU202301960

doi:10.6342/NTU202301960

doi:10.6342/NTU202301960

Lists of Figures

doi:10.6342/NTU202301960

doi:10.6342/NTU202301960

doi:10.6342/NTU202301960

doi:10.6342/NTU202301960

Lists of Tables

doi:10.6342/NTU202301960

Chapter 1 Introduction

1.1 Properties of Indium Selenide (InSe)

Indium selenide (InSe) is an emerging layered semiconductor material that is held together by weak van der Waals forces between its layers. InSe has been studied that it has well electronic, optoelectronic and deformability, which make it applied on variety of devices. [1-3] Owing to its potential application on flexible device, it becomes important to know strain effects on the properties of InSe. In this study, we are interested in the strain effects on the second harmonic generation (SHG) from InSe.

A monolayer InSe is composed of indium and selenide atoms arranged in a hexagonal lattice structure. It can be categorized into two directions, which are armchair and zigzag, by checking the sequence of indium and selenide atoms. The zigzag direction in monolayer InSe is composed of the same type of atoms such as all selenide or all indium atoms. The armchair direction is characterized by the sequence of Se-In-Se-In, as shown in Fig 1-1. A studied has shown that the SHG technique can reveal hexagonal structure of monolayer InSe by detecting specific polarization of the signal. [4] While the laser polarization is parallel to the armchair direction, the SHG signal with the same polarization direction will be strongest. When rotating a monolayer of InSe and detecting the SHG signal with polarization parallel to incident polarization, six armchair directions

doi:10.6342/NTU202301960

can be observed in a full cycle, resulting in a six-fold petals pattern in the angle-SHG relationship, which is called angle-resolved SHG pattern (shown in Fig 1-1).

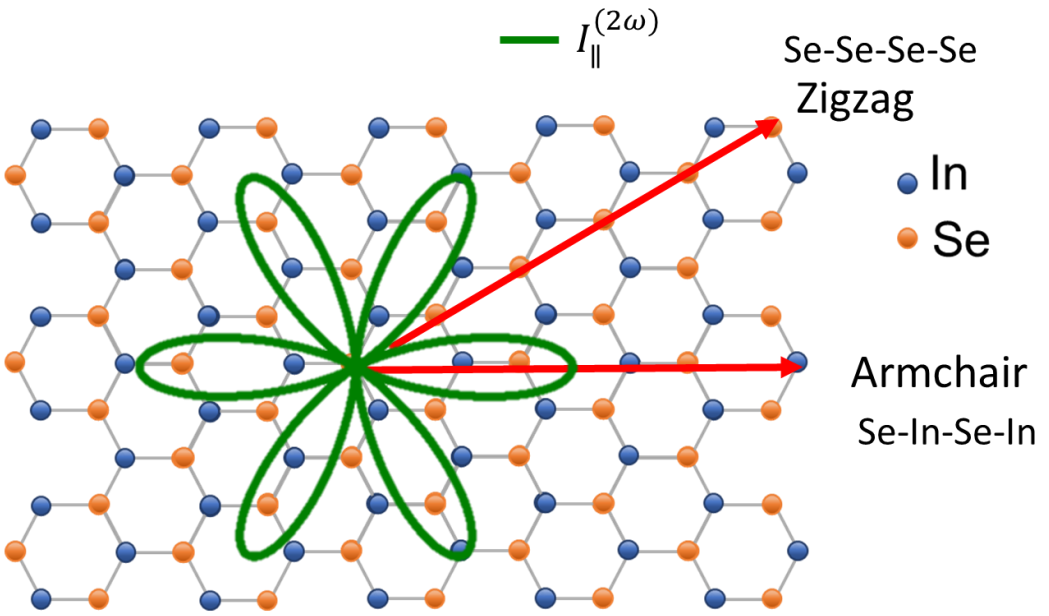

Fig 1-1 The schematic structure of monolayer InSe includes both the zigzag and armchair directions. The green line depicts the intensity of SHG signal with polarization parallel to the incident laser polarization, which denoted as $I_{\parallel}^{(2\omega)}$.

Research has demonstrated that bulk InSe exhibits polytypes due to different stacking, including that β and ε phases with AB stacking mode, and the γ phase with ABC stacking mode [5-8] (As shown in Fig 1-2). To identify the phase of an InSe crystal, a recent study has demonstrated that the oblique incident SHG technique can distinguish different stacking modes due to its structure sensitive property. [9] For β phase, its

doi:10.6342/NTU202301960

centrosymmetric structure makes it forbidden to generate the second harmonic signal. As for γ and ε phase, although they are both non-centrosymmetric structure which make it easily generate the second harmonic signal, the zero second-order polarization along z direction of ε stacking mode makes it possible to be distinguished from the γ stacking mode.

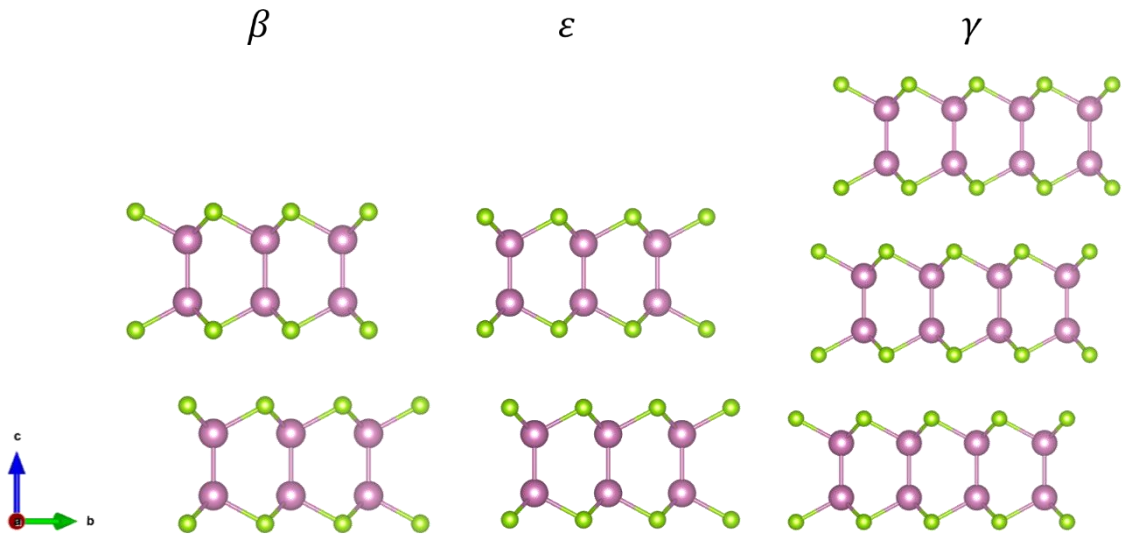

Fig 1-2 Different stacking modes of InSe. [10] The green atoms are Se and purple atoms are In.

In the experiment, we use the oblique incident technique to confirm the investigated InSe crystal is γ phase which belongs to C_{3v} point group. [11] The few-layers InSe flakes were prepared by mechanically exfoliation and placed on a flexible substrate. To study the strain effect, we applied uniaxial compressive strain along the armchair

doi:10.6342/NTU202301960

direction of the InSe flake and detected its second harmonic generation signal. The results show the intensity of SHG from InSe few-layers decreases while the compressive strain level increases.

1.2 Strain Engineering and Optical Tools for Strain Measurement

Strain engineering is an important field in material science, as it enables the tuning of electronic and optoelectronic properties of materials by the external mechanical strain. The use of two-dimensional atomic crystals as a versatile platform to study the impact of strain is a promising approach, as they can withstand large deformations without breaking down. While conducting the strain engineering and investigate the material properties, quantitatively knowing the strain magnitude applied on the material is an important issue.

Several techniques have been developed to measure the strain on materials in recent years, including optical techniques such as photoluminescence (PL), Raman spectroscopy, and second harmonic generation (SHG). PL measurement reflects the change in the band structure of the material under strain, while both Raman and SHG are crystal-structure-related optical responses. In the case of Raman spectroscopy, it has been primarily studied the peak positions and intensities of Raman modes with the influence of strain. As for the SHG technique, most of the studies have focused on the relationship between strain and angle-resolved SHG patterns.

It has been demonstrated that polarized Raman spectroscopy can provide

doi:10.6342/NTU202301960

information about the crystal orientation and even the strain direction [12,13] . In other words, both Raman and SHG techniques possess the capability to resolve the strain distribution on the material. However, it is more time-efficient by using SHG technique to study the strain effect on the small InSe flake because InSe can generate strong second harmonic signal due to its non-centrosymmetry structure. Besides, according to the research conducted by Lukas Mennel et al, the spatial resolution (280 nm) of their SHG setup is below the diffraction limit of the excitation wavelength (800 nm), which is higher than the strain mapping techniques of PL or Raman [14] . Therefore, it is possible to achieved high-resolution measurement of strain distribution on the material by using angle-resolved SHG technique.

1.3 Second Harmonic Generation (SHG) and Strain

Second harmonic generation (SHG) is a nonlinear optical process. From the phenomenological perspective, the SHG process is that two photons of the same frequency are converted into a single photon with the double frequency and half of the wavelength. This process occurs in the material lacking inversion symmetry because it originates from the interaction between the electrons inside the material and the external electric field [15]. When a non-centrosymmetric material is subjected to a strong electric field, the electrons within the material absorb the energy of the field and begin to oscillate. Due to the non-symmetric potential well that confines the electrons, their motion becomes

doi:10.6342/NTU202301960

non-harmonic oscillation in nature. This non-harmonic oscillation causes the electrons to emit high-order electromagnetic waves, which can be classified based on their frequency, and produces the nonlinear polarization in the material. Second harmonic generation is related to the second-order displacement of the electrons. In the material with inversion symmetry or centrosymmetric structure, the electrons are confined to a symmetric potential well, resulting in a second-order displacement of zero. [16] Therefore, the second harmonic generation cannot be observed in such symmetric structure.

Due to the structure-sensitive property, second harmonic generation technique can be used to determine the orientation of crystal and even monitor strain on the material [17]. For example, monolayer transition metal dichalcogenides materials, such as MoS_2,WS_2,and WSe_2 are hexagonal structure. Their angle-resolved SHG patterns are six-fold when the parallel or perpendicular polarization of SHG signals are detected. [18-20] The six-fold symmetry pattern is related to the hexagonal structure and the maximum and minimum intensities correspond to the armchair and zigzag direction if the parallel signal is detected. For strain measurement, a research demonstrated that the direction and magnitude of strain can be obtained by measuring the angle-resolved SHG pattern from the two-dimensional (2D) MoS_2 material [14]. The researchers applied uniaxial strain to 2D MoS_2 and manipulated the polarizations of both the laser and second harmonic signal to align them parallel to each other, while also rotating the polarization of laser to

doi:10.6342/NTU202301960

probe the second harmonic signal in different rotational angle. They observed that while the in plane uniaxial strain applied on different direction, the corresponding angle-resolved SHG pattern becomes different. By analyzing the different angle-resolved patterns, they are able to obtain the strain vector on the material. Our research focuses on investigating changes in the angle-resolved second harmonic generation of InSe while it was applied uniaxial strain.

1.4 The Strain Transfer Efficiency

During the literature review, it was found that the strain transfer efficiency is related to the Young's modulus of the substrate. When the Young's modulus of the substrate is higher, the strain transfer efficiency is better [21]. This means that the calculated strain on the substrate is closer to the actual strain on the material. In addition, there are studies that compare the strain transfer efficiency of polydimethylsiloxane (PDMS) and polyvinyl alcohol (PVA) substrates. PDMS has a Young's modulus of approximately 430 KPa, whereas PVA has a Young's modulus of around 650 MPa. The results showed that the strain transfer efficiency of PDMS is about 10%, while that of PVA is 60% [22]. Therefore, we referred to a study that investigated strain and second harmonic effects [23], and used a polyethylene naphthalate (PEN) substrate with a layer of photoresist (SU-8) on top to make the surface smoother. The Young's modulus of the photoresist is about 2.4-5.5 GPa [24], which is expected to result in better strain transfer efficiency for this

doi:10.6342/NTU202301960

substrate.

1.5 Frist-Principles and Second Harmonic Generation (SHG)

First-principles calculation is a powerful computational method used in materials science, chemistry, and physics to predict the properties and behavior of materials from fundamental physical principles. In condense matter physics, it is usually used to study the electronic properties, such as the band structure, of materials, which can be metal, semiconductor, and insulator. Because first-principles calculation is based on fundamental physical principles rather than empirical data or assumptions, it can be used to predict the properties of material that have not yet been studied experimentally. In this study, we used first-principles method to theoretically understand the strain effect on second harmonic generation from InSe.

The first-principles method used to calculate the band structure of InSe is based on density functional theory (DFT), generalized gradient approximations (GGA) [25], norm-conserving pseudopotentials [26] and optimized pseudoatomic basis functions [27]. The calculations were conducted with the assistance of OpenMX code [28]. Because the DFT usually underestimates the band gap of materials [29], it is necessary to modify band energy. Here, we performed the scissor operation to modify the calculated band gap so as to make it close to the measured energy band gap. After obtaining the band structure, we calculated the second-order susceptibility by using the formula derived by Sipe et al.

doi:10.6342/NTU202301960

[30,31] To study the strain effect, the unit cell of InSe will be modified according to the desired strain before calculating the band structure.

The calculation results showed a linear relationship between strain and second-order susceptibilities, with a decrease in susceptibility as strain increased. However, the calculated strain effect was not as significant as the experimental results. To improve the agreement between theory and experiment, the first-principles results were modified with a correction term multiplying with the slopes from the linear relationships. As a consequence, the theoretical and experiment results agree well with each other.

doi:10.6342/NTU202301960

Chapter 2 Methods

2.1 Experiment Setup for Second Harmonic Generation and Signal Confirmation

The schematic diagram of the experiment setup is shown in Fig 2-1. In order to induce the nonlinear optical effect, the Ti:Sapphire pulse laser with central wavelength ~790 nm was used to provide the strong electric field. Along the beam path, two sets of half-wave plate (HWP) and polarization beam splitter (PBS) were used to adjust the laser power. Considering the dispersion will decrease the SHG transferring efficiency, we used a compressor to compress the pulse wavelength so as to maximize the SHG signal. An inverted microscope system integrating with a scanning system is able to measure two-dimensional SHG image. The scanning system is made of two galvo-mirrors such that it can direct the beam along x and y directions. Before the beam goes into the scanning system, a linear polarizer was set to purify the incident laser polarization. A long working distance objective lens (20x, NA=0.35) was selected in the purpose of preventing from touching the substrate even it was curved. While the laser shine on the sample, a dichroic mirror in the microscope allows the beam with wavelength shorter than 600 nm transmit and reflects the fundamental beam with longer wavelength. While the beam went outside of the microscope, it would go through a linear polarizer, a bandpass filter and eventually be detected by single-photon-counting photomultiplier (PMT). The linear polarizer was

doi:10.6342/NTU202301960

used to select the certain polarization of the SHG signal and the bandpass filter could block the leakage from the fundamental beam.

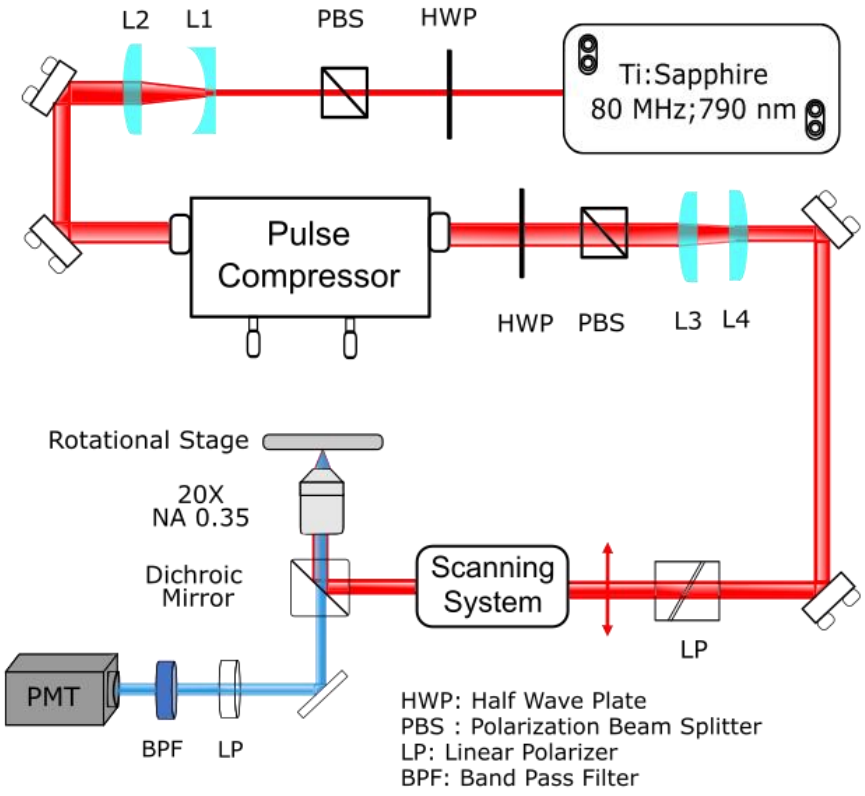

Fig 2-1 The schematic diagram of experiment setup.

In this study, we mainly analyze the angle-resolved SHG pattern to realize the strain effect on few-layers InSe. To obtain the angle-resolved SHG pattern, the sample was fixed on a motorized rotational stage (Newport, URS150BCC), which was placed on the inverted microscope and set for stepping 10 degrees for each SHG image measurement.

In the aspect of signal confirmation, there are several methods can check if the

doi:10.6342/NTU202301960

detected signal is truly from the second harmonic generation. First, we checked the spectrum of the signal to know whether its wavelength is half of the incident pulse laser wavelength. Second, we can conduct the power dependent measurement. Because the intensity of second harmonic generation signal is proportion to the square of the incident power, we can use power dependent measurement to know if the detected signal obeys this relation. The third method is to conduct the angle-resolved SHG measurement to know if the pattern agrees well to the structure of the InSe. For normal incident condition, we can determine the polarization of the detected signal by the polarizer in front of the PMT. In the case of detected signal polarization parallel or perpendicular to incident polarization, the angle-resolved SHG pattern shows $\cos^2 3\theta$ or $\sin^2 3\theta$ which is six-fold rotational symmetric pattern. (See section 3.1.2) The signal can be confirmed to be second harmonic generation if the angle-resolved pattern of parallel or perpendicular signal is six-fold rotational symmetry.

2.2 Phase Identification by Oblique Incident Second Harmonic Generation (SHG) Measurement

Bulk InSe has different phases because of the different stacking sequence along z-direction. In order to probe the difference along z-direction, the oblique incident SHG technique, which allows to detect the information with z-polarization, was consider to identify the phase of the studied material. The schematic diagram of the experiment setup

doi:10.6342/NTU202301960

is shown in Fig 2-2. The oblique incident geometry was achieved by setting the optical components vertically and the mirrors were set to direct the beam incident with 45° incident angle. Along the incident light path, we put a linear polarizer to choose a specific incident linear polarization and a convex lens with focal length 50 mm to focus the beam on the sample. To make sure the all signal was collected while the sample is in different rotational angle, two lenses were used to converge the light into an analog photomultiplier (PMT). A linear polarizer and a 400 nm bandpass filter with 40 nm band were placed before the PMT to select a specific polarization and purify the SHG signal. While conducting the angle-resolved SHG measurement, the measuring position of the sample was expected to be the same. Therefore, the sample stage was integrated with two 2D manual stages and a rotational stage in the middle to increase the degrees of freedom. The bottom 2D stage was used to make the laser position align with the rotational center. Once the alignment was achieved, we are able to search a suitable position to measure signal by moving the top 2D stage.

doi:10.6342/NTU202301960

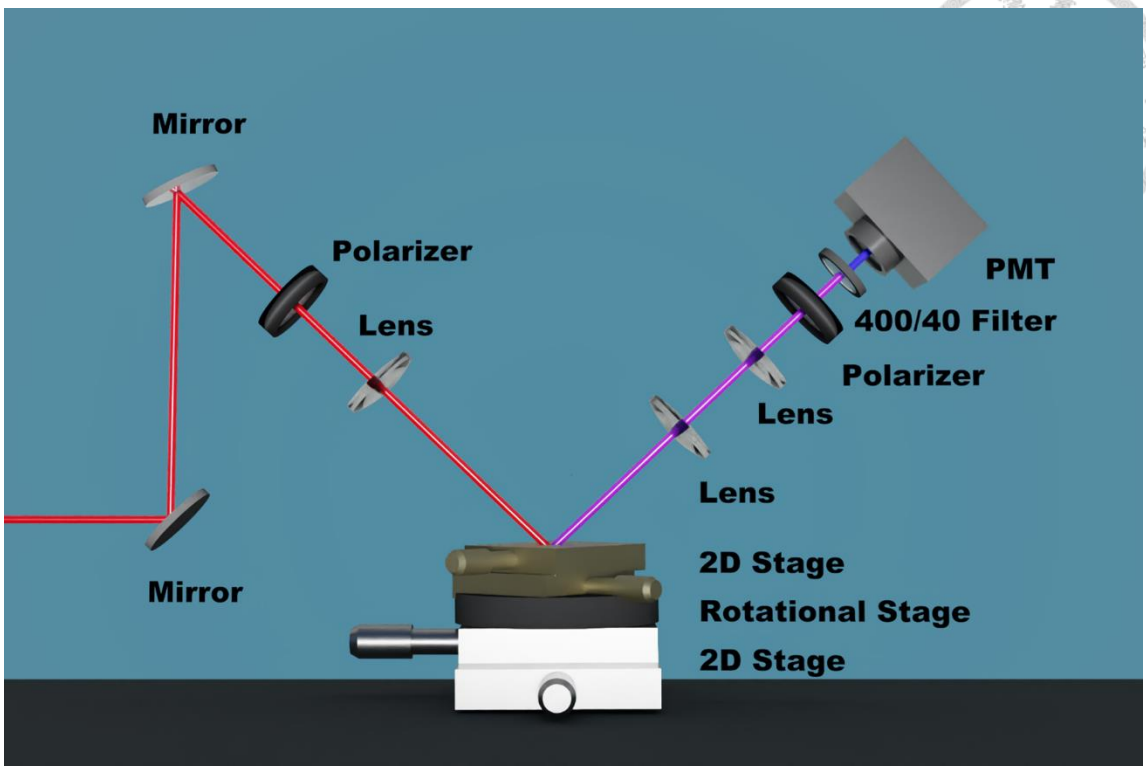

Fig 2-2 The schematic diagram of oblique incident experiment setup.

2.3 Preparation of PDMS (Polydimethylsiloxane)

In this experiment, we utilized the exfoliation method to prepare few-layers InSe. To accomplish this, we employed a silicon-based elastomer, polydimethylsiloxane (PDMS), to peel the layers of InSe from the bulk crystal. The PDMS was prepared by mixing the base and curing agent in a 10:1 weight ratio, and the resulting mixture was thoroughly stirred by using an electric drill. After stirring, the liquid was poured into a Petri dish and placed in a vacuum chamber to remove any bubbles. To expedite the solidification process, the Petri dish was then placed on a heating plate. The PDMS was cured completely at a temperature of 90°C, which took approximately 40 minutes.

doi:10.6342/NTU202301960

2.4 Flexible Substrate Preparation

For the strain dependence experiment, a flexible substrate is necessary to transfer the deformation onto the small sample. Considering the strain transfer efficiency, we chose the polyethylene naphthalate (PEN) substrate coated with photoresist, SU-8, on top. The PEN substrate was cut to be 3×3 centimeter square then put into a beaker. The substrate was cleaned by ultrasonic cleaning with a series of solvent including acetone, isopropyl alcohol (IPA) and deionized water. Each solvent was subjected to 10 minutes of 37 kHz ultrasound treatment to ensure thorough cleaning. After the cleaning process, the substrate was put into a spin coater then covered by 1.5 ml SU-8 liquid. The parameters for spin-coating process as shown in Table 2-1. Afterward, the substrate was put on a heating plate with temperature at 200 °C to heat up for 30 minutes for making the SU-8 thin film stick on the PEN. The thickness of the coated substrate is approximately 125 μm.

doi:10.6342/NTU202301960

Table 2-1 The spin-coating parameters.

Steps	Time (s)	Frequency (rpm)
1	5	500
2	5	1000
3	5	1500
4	5	2000
5	5	2500
6	30	2500

2.5 Sample Fabrication and Characteristics

The InSe crystal is provided by Dr. Raman Sankar in institute of physics, Academia Sinica. They grew the InSe crystal by the vertical Bridgman method. The 99.999% pure Indium (In) and Selenide (Se) chemicals were purchased from Sigma Aldrich. The growth process involved mixing In and Se powders in quartz ampoules under a vacuum of 10^{-4} Pa. Afterward, the ampoules were kept in a horizontal furnace at 550 °C for two days to achieve a partially mixed crystal. The mixed crystals were then used to grow the pure InSe single crystal using a vertical Bridgman setup. During the Bridgman process, the furnace was maintained at a high temperature of about 850 °C. The mixed crystal in the ampoule was heat-treated at 850 °C for 24 hours until it melted entirely. To obtain a

doi:10.6342/NTU202301960

large-sized single crystal, the ampoules were gradually lowered through a temperature gradient of 1 °C at a rate of 0.1 mm/h. By using this procedure, they obtained InSe single crystals in bulk with over 5 cm long and 1 cm in diameter.

The crystal was characterized by Raman spectroscopy and its band gap was determined by measuring the photoluminescence (PL). Both Raman and PL measurements were conducted by using a 532 nm continuous-wave laser as the excitation source. The sample was illuminated by the laser and the signal with fundamental laser was reflected out of the microscope. A 532 nm long pass filter was used to filter out the fundamental laser beam and allow the signal transmit so as to be directed into spectrometer (Horiba, iHR550).

Due to the weak van der Waals force between layers, few-layers InSe was easily prepared by exfoliation method. The studied InSe flakes were exfoliated from the crystal by PDMS and transferred to the center of flexible, transparent and square substrate, PEN with SU-8 on top by stamping procedure. In order to select the few-layers flake, we used microscope to record the optical contrast of flakes. The lower contrast means the thickness of the sample is thinner. Therefore, we browsed the exfoliated flakes by microscope and selected the target sample with low optical contrast. The thickness of the target sample was precisely measured by atomic force microscopy.

After finding the target samples, we conducted angle-resolved SHG measurement to

doi:10.6342/NTU202301960

figure out the armchair direction of the target sample. To apply the uniaxial strain along armchair direction of the sample, the substrate was marked along the armchair direction and cut into rectangular shape with the longer side parallel to the armchair direction.

2.6 Strain Device and Strain Estimation

In this experiment, we intended to deform the substrate in order to apply strain on the InSe flake. By referring to the work from Island et al [32] , a strain device was designed to fix and bend the substrate. The schematic is shown in Fig 2-3. We put the substrate on the two movable stages and moved the two sides of substrate toward the center of the strain device. The right and left shorter side of the substrate were clamped by two aluminum blocks respectively.

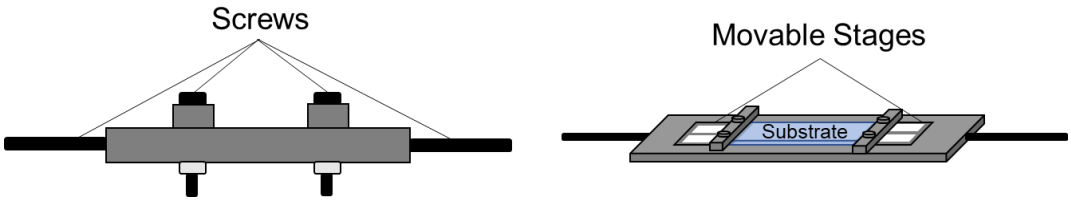

Fig 2-3 The schematic of self-designed strain device.

While the substrate was fixed, we could rotate the screws to change the position of movable stages. In this way, the substrate would be curved as an arch bridge. The schematic of curved substrate is shown in Fig 2-4.

doi:10.6342/NTU202301960

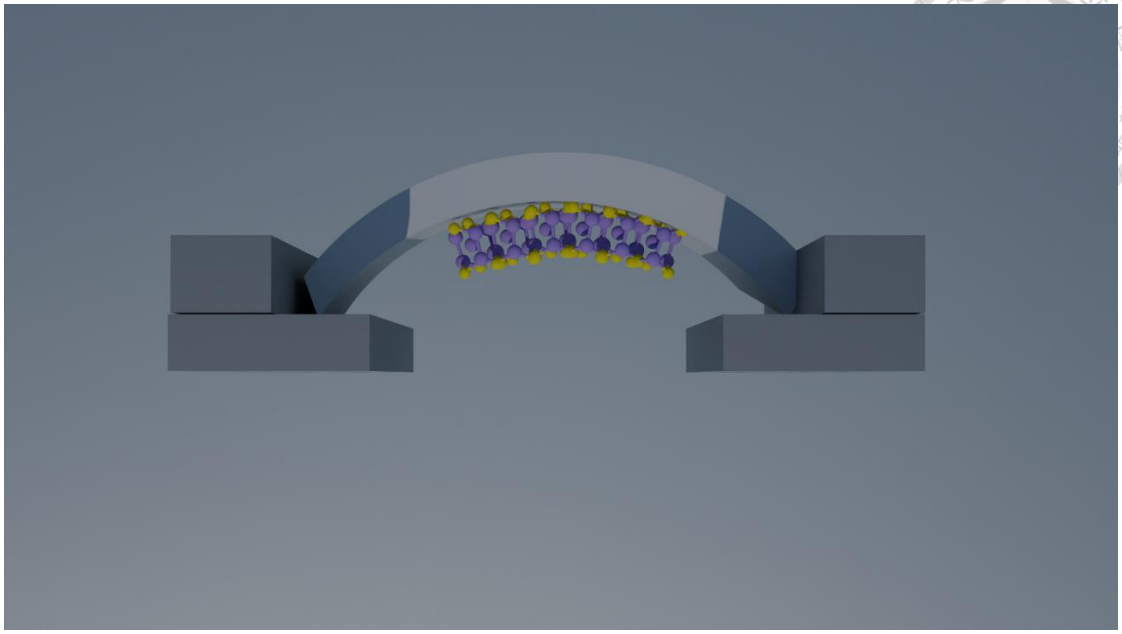

Fig 2-4 The schematic of curved substrate.

Because the size of the InSe flake is in microscopic scale, the strain can be estimated through small angle approximation. The definition of strain is

$$\varepsilon = \frac{\Delta L}{L}, \tag{2.1}$$

which ε is strain, ΔL is the change in length and L is the original length. Assume the thickness of substrate is d, the radius of curvature of curved substrate is R and the radian to cover the sample size is θ. The original length L can be approximated to be $R\theta$. To applied the compressive strain, the sample would be placed in the inner side of the substrate where the radius of curvature is less than the original radius with half of the thickness, i.e. $\mathrm{R} - \frac{\mathrm{d}}{2}$, such that the final length of the material is $(\mathrm{R} - \frac{\mathrm{d}}{2})\theta$. Therefore, the compressive strain is

doi:10.6342/NTU202301960

$$\varepsilon = -\frac{d}{2R}. \quad (2.2)$$

The schematic diagram is shown in Fig 2-5.

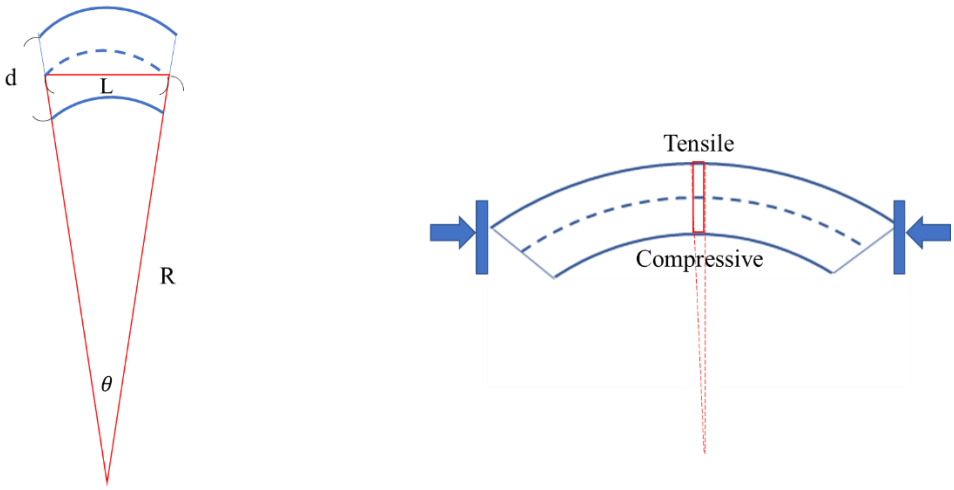

Fig 2-5 The schematic of the strain approximation. In this figure, L represents the original length of the sample size.

2.7 First-Principles Calculation

The first-principles calculation based on density functional theory (DFT) was conducted with the assistance of OpenMX code. The programs to conduct the calculation are provided by Dr. Chi-Cheng Lee in department of physics, Tamkang University. In the calculation process, generalized gradient approximations (GGA), norm-conserving pseudopotentials and optimized pseudoatomic basis functions were considered.

The first step for the calculation is setting the unicell of the investigated material. To

doi:10.6342/NTU202301960

construct the structure of γ phase InSe, a unicell consisting of three InSe monolayers in an ABC stacking order was used and the crystal x-axis was defined as armchair (AC) direction. For the atomic basis functions, In7.0-s3p2d2 and Se7.0-s3p2d2 were adopted, which 7.0 is the cutoff radius and s3p2d2 means three s-orbitals, two p-orbitals and two d-orbitals. Numerical integrations and the solution of the Poisson equation were performed using a cutoff energy of 500 Ry. The first Brillouin zone was discretized with 8×8×2 sampling points in k-space.

During the calculations, only the components of the lattice vectors associated with the desired strain were fixed, and the structures were fully relaxed without taking spin-orbit coupling into account. For the unstrained ground-state structure, no constraint was applied to the lattice vectors. After obtaining the optimized lattice constants, the atomic positions were relaxed again with the effect of spin-orbit coupling. The resulting lattice met the criterion of having atomic forces smaller than 0.0001 Ha/bohr. By setting the electronic self-consistent field (SCF) criterion to 10^{-9} Ha, the difference between the band energies in the last two consecutive SCF steps was ensured to be smaller than the criterion.

To calculate the SHG susceptibilities, the momentum matrix elements were used along with the basis of the adopted pseudoatomic basis functions [33]. The formula derived by Sipe et al. for the independent-particle approximation was followed. A 60 ×

doi:10.6342/NTU202301960

60 × 8 k-point sampling was used to obtain the SHG susceptibilities, with a broadening parameter of η = 0.1 eV. The electronic temperature was set to 300 K for all SCF and SHG calculations, based on the Fermi–Dirac distribution function.

doi:10.6342/NTU202301960

Chapter 3 Calculation Results

3.1 Mathematical Description of Angle-Resolved Second Harmonic Generation for C_{3v} Point Group

3.1.1 General Description

The nonlinear optical effect originates from the nonlinear polarization terms of the material. The power expansion of the material polarization $\boldsymbol{P}$ is

$$\boldsymbol{P} = \boldsymbol{P^{(1)}} + \boldsymbol{P^{(2)}} + \boldsymbol{P^{(3)}} + \cdots \propto \chi^{(1)}\boldsymbol{E} + \chi^{(2)}\boldsymbol{E}^2 + \chi^{(3)}\boldsymbol{E}^3 + \cdots, \quad (3.1)$$

which $\chi^{(n)}$ is the nth order susceptibility and $\boldsymbol{E}$ is the external electric field. The second harmonic generation is related to the second term of the expansion. The second-order polarization $\boldsymbol{P}^{(2)}$ is

$$P_l^{(2)} \propto \sum_{mn} \chi_{lmn}^{(2)} E_m E_n, \quad (3.2)$$

which the indices l, m and n represent the directions in cartesian coordinate. In equation (3.2), $\chi_{lmn}^{(2)}$ is a third-rank tensor and its nonzero components are determined by the structure of material [34]. In the case of second harmonic generation, the external electric fields E_m and E_n have the same frequency such that it remains the same result if the indices m and n exchange. Therefore, the third-rank tensor can be contracted to a 3×6 matrix and we defined d_{lk} as the notation of the matrix element. The index k

doi:10.6342/NTU202301960

can be 1, 2, 3, 4, 5 and 6 which represents to xx, yy, zz, yz (zy), xz (zx), and xy (yx). In this work, the studied material, γ-phase InSe, belongs to C_{3v} point group, and the corresponding d-matrix is [16]

$$d = \begin{pmatrix} d_{11} & -d_{11} & 0 & 0 & d_{15} & 0 \\ 0 & 0 & 0 & d_{15} & 0 & -d_{11} \\ d_{31} & d_{31} & d_{33} & 0 & 0 & 0 \end{pmatrix}. \quad (3.3)$$

We rewrite equation (3.2) in matrix representation as

$$\begin{pmatrix} P_x^{(2)} \\ P_y^{(2)} \\ P_z^{(2)} \end{pmatrix} = \begin{pmatrix} d_{11} & -d_{11} & 0 & 0 & d_{15} & 0 \\ 0 & 0 & 0 & d_{15} & 0 & -d_{11} \\ d_{31} & d_{31} & d_{33} & 0 & 0 & 0 \end{pmatrix} \begin{pmatrix} E_x^2 \\ E_y^2 \\ E_z^2 \\ 2E_yE_z \\ 2E_xE_z \\ 2E_xE_y \end{pmatrix}, \quad (3.4)$$

which E_x, E_y and E_z are the external electric filed in cartesian coordinates. The relation between second-order polarization $\boldsymbol{P}^{(2)}$ and SHG intensity is

$$I_{tot}^{(2\omega)} \propto \left|\boldsymbol{P}^{(2)}\right|^2, \quad (3.5)$$

which $I_{tot}^{(2\omega)}$ is the total intensity of SHG signal. In order to probe the structure of the crystal, the intensity with particular polarization was measured. To calculate the intensity with particular polarization, equation (3.5) is modified as

$$I^{(2\omega)} \propto \left|\boldsymbol{e}^{2\omega}\boldsymbol{P}^{(2)}\right|^2, \quad (3.6)$$

which $\boldsymbol{e}^{2\omega}$ is a vector and denotes the polarization of the SHG intensity.

doi:10.6342/NTU202301960

3.1.2 Normal Incident Condition

For normal incident condition, the z-component of the external electric field is zero. We define that the rotation angle θ is between the linear polarization direction and the crystal x- axis. Therefore, the external electric field vector is

$$\begin{pmatrix} E_x^2 \\ E_y^2 \\ E_z^2 \\ 2E_yE_z \\ 2E_xE_z \\ 2E_xE_y \end{pmatrix} \propto \begin{pmatrix} \cos^2\theta \\ \sin^2\theta \\ 0 \\ 0 \\ 0 \\ 2\sin\theta\cos\theta \end{pmatrix}. \quad (3.7)$$

By substituting equation (3.7) to the equation (3.4), we get the second-order polarization as

$$\begin{pmatrix} P_x \\ P_y \\ P_z \end{pmatrix} \propto \begin{pmatrix} d_{11}\cos 2\theta \\ -d_{11}\sin 2\theta \\ 0 \end{pmatrix}. \quad (3.8)$$

In this work, the SHG intensity with the polarization parallel and perpendicular to the incident light were measured, which is denoted as $I_{\parallel}$ and $I_{\perp}$ respectively. The parallel polarization vector is $\boldsymbol{e}_{\parallel}^{(2\omega)} = (\cos\theta, \sin\theta, 0)$ and the perpendicular polarization vector is $\boldsymbol{e}_{\perp}^{(2\omega)} = (\sin\theta, -\cos\theta, 0)$. By using the equation (3.6), we can get the $I_{\parallel}^{(2\omega)}$ and $I_{\perp}^{(2\omega)}$ as

$$I_{\parallel}^{(2\omega)} \propto \left| P_x^{(2)}\cos\theta + P_y^{(2)}\sin\theta \right|^2 = d_{11}^2\cos^2 3\theta. \quad (3.9)$$

$$I_{\perp}^{(2\omega)} \propto \left| P_x^{(2)}\sin\theta - P_y^{(2)}\cos\theta \right|^2 = d_{11}^2\sin^2 3\theta \quad (3.10)$$

doi:10.6342/NTU202301960

Equation (3.9) and (3.10) indicate $I_{\parallel}^{(2\omega)}$ and $I_{\perp}^{(2\omega)}$ is the function of $\cos^2 3\theta$ and $\sin^2 3\theta$. Both of them are show the six-fold symmetry if they were plot in polar form as shown in Fig 3-1.

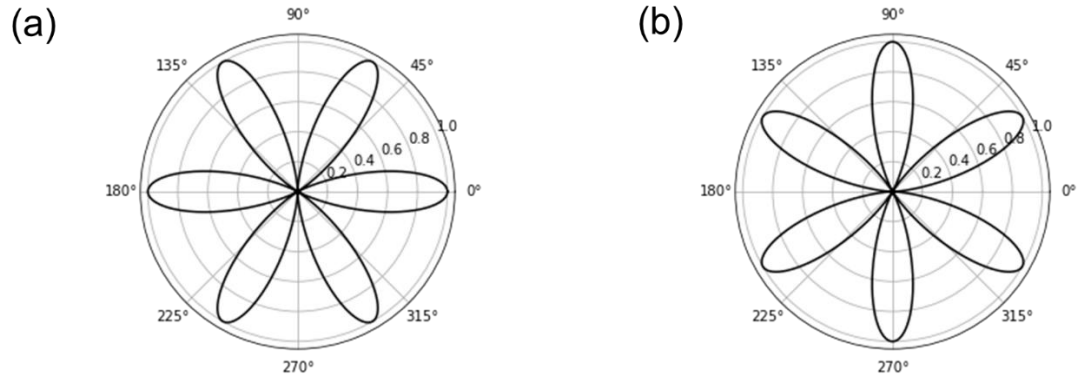

Fig 3-1 The polar plots of $\cos^2 3\theta$ (a) and $\sin^2 3\theta$ (b)

3.1.3 Oblique Incident Condition

Compare with the normal incident condition, we can get much more information by using oblique incident geometry because the incident light and the response have an additional component along z-direction. For the oblique incident geometry, the polarization direction can be chosen as parallel (denoted as P) and perpendicular (denoted as S) to the incident plane. Assuming the incident angle is ϕ and the rotation angle of the crystal is θ, the electric field vectors with P-polarization ($\boldsymbol{E}_P$) and S-polarization ($\boldsymbol{E}_S$) are

doi:10.6342/NTU202301960

$$\boldsymbol{E}_P = (-\cos\theta\cos\phi\,, -\sin\theta\cos\phi\,, \sin\phi), \quad (3.11)$$

and

$$\boldsymbol{E}_S = (-\sin\theta\,, \cos\theta\,, 0). \quad (3.12)$$

There are also p-polarization ($\boldsymbol{e}_P^{2\omega}$) and s-polarization ($\boldsymbol{e}_S^{2\omega}$) for SHG response and can be described as follows

$$\boldsymbol{e}_P^{2\omega} = (\cos\theta\cos\phi\,, \sin\theta\cos\phi\,, \sin\phi), \quad (3.13)$$

and

$$\boldsymbol{e}_S^{2\omega} = (-\sin\theta\,, \cos\theta\,, 0). \quad (3.14)$$

The resulting angle-resolved SHG intensities in different configurations are

$$I_{pp} \propto (d_{11}\cos^3\phi\cos 3\theta + (-2d_{15} + d_{31})\cos^2\phi\sin\phi + d_{33}\sin^3\phi)^2, \quad (3.15)$$

$$I_{ss} \propto (d_{11}\sin 3\theta)^2, \quad (3.16)$$

$$I_{ps} \propto (d_{11}\sin 3\theta\cos^2\phi\,)^2, \quad (3.17)$$

$$I_{sp} \propto (-d_{11}\cos\phi\cos 3\theta + d_{31}\sin\phi)^2, \quad (3.18)$$

which I_{mn} represents the intensity resulting from the combination of input polarization m and output polarization n.

In this study, we used oblique incident geometry to get the information about the z-

doi:10.6342/NTU202301960

direction so as to determine the phase of the bulk InSe. It is noted that the equation (3.3) describes the feature of C_{3v} point group, which is the geometry of γ-InSe. For the case of ε-InSe, which belongs to D_{3h} point group in its bulk form, the differences compared to the d-matrix of the γ phase are in the matrix elements containing the z-component. Because the ε-InSe exhibits inversion symmetry along the z-direction, the z-related elements of its d-matrix are zero. As the consequence, there is no difference between the normal and oblique incident SHG measurement in the case of ε phase InSe. The non-zeros elements containing only x- and y-components for ε phase are exactly the same as those in the γ phase of InSe. The evidence for determining the phase of the studied material is to investigate the angle-resolved SHG pattern in both normal and oblique incident condition and compare the symmetry of the pattern.

Before setting the experiment setup, we needed to determine the incident angle and the type of the polarization combination to make sure the stacking sequence. Therefore, we simulated the angle-resolved patterns for the four different combinations by using the d-matrix for C_{3v} point group in equation (3.3) with the incident angle range from $25°$ to $45°$ and they are shown in Fig 3-2. We denoted the incident polarization as Pin or Sin and the polarization of detected signal as Pout or Sout such that there are 4 combinations of the incident and output polarization. We can observe that the angle-resolved SHG patterns for Sin-Sout and Pin-Sout cases are the six-fold symmetry regardless of the

doi:10.6342/NTU202301960

incident angle. As for the Sin-Pout condition, the symmetry of the pattern doesn't change significantly even though it includes the effect of d_{31} component. While for the Pin-Pout condition, it appears three-fold symmetry starting at $35°$ incident angle. According to these results, the measurement condition that can distinguish the phase of InSe should be Pin-Pout configuration with the large incident angle.

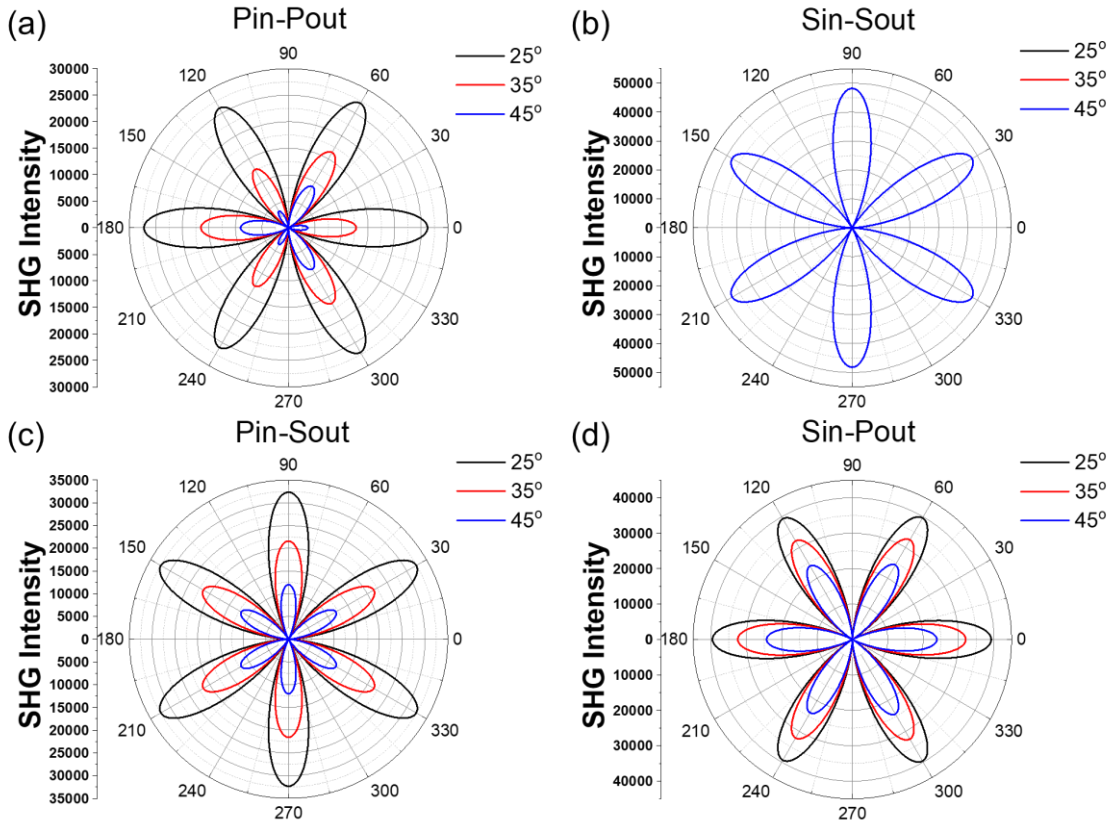

Fig 3-2 The P-in P-out (a), S-in S-out (b), P-in S-out (c) and S-in P-Pout (d) polar plots of SHG intensity with incident angle $25°$, $35°$ and $45°$.

doi:10.6342/NTU202301960

3.2 First-Principles Calculation Results

3.2.1 Band Structure under Different Strain Cases

Using the approach outlined in Sec. 2.7, we conducted the calculation of the band structure of γ-InSe under varying degrees of strain (ranging from 0% to -2%). Our findings are presented in Fig 3-3 through Fig 3-7 (a). To provide a visual representation of the corresponding structures, we utilized VESTA to generate the structure plots displayed in Fig 3-3 through Fig 3-7 (b). For distinguishing the differences of the structure in each strain cases, the angles between atoms are labeled on the structures.

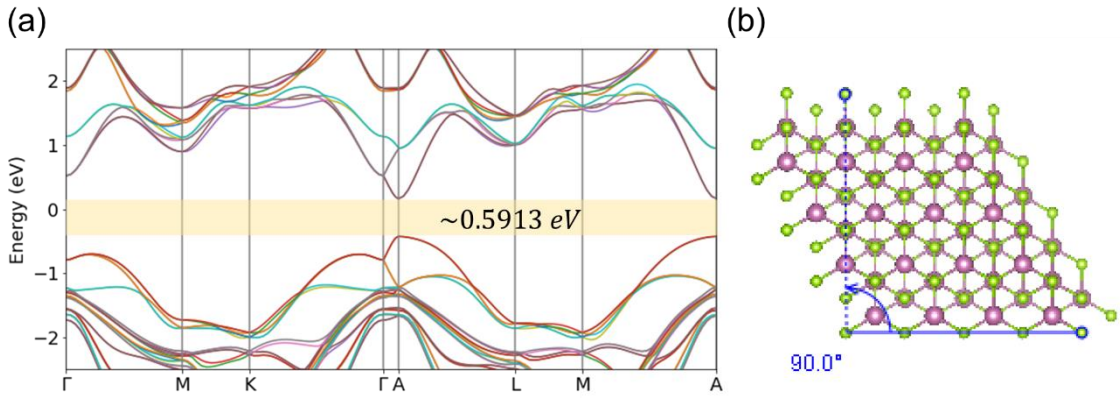

Fig 3-3 Band structure (a) and crystal structure (b) of unstrained InSe. The green atoms are Se and purple atoms are In.

doi:10.6342/NTU202301960

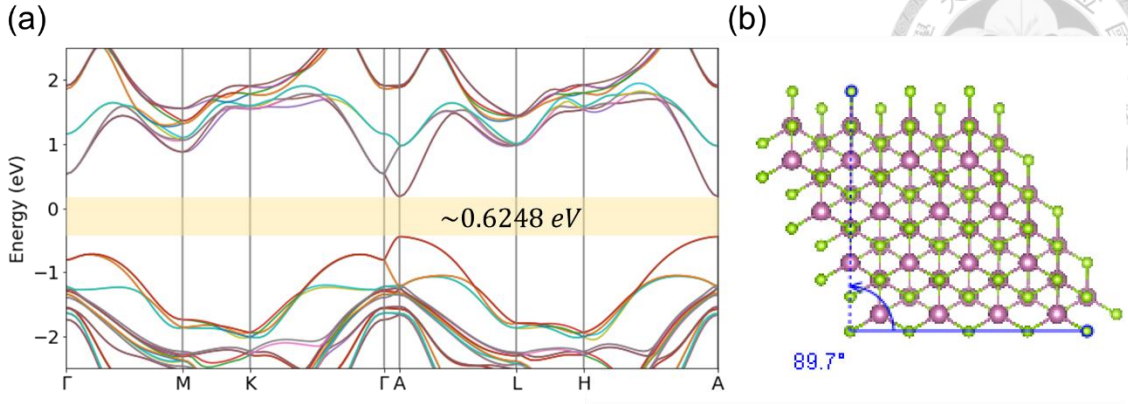

Fig 3-4 Band structure (a) and crystal structure (b) of InSe with -0.5% strain. The green atoms are Se and purple atoms are In.

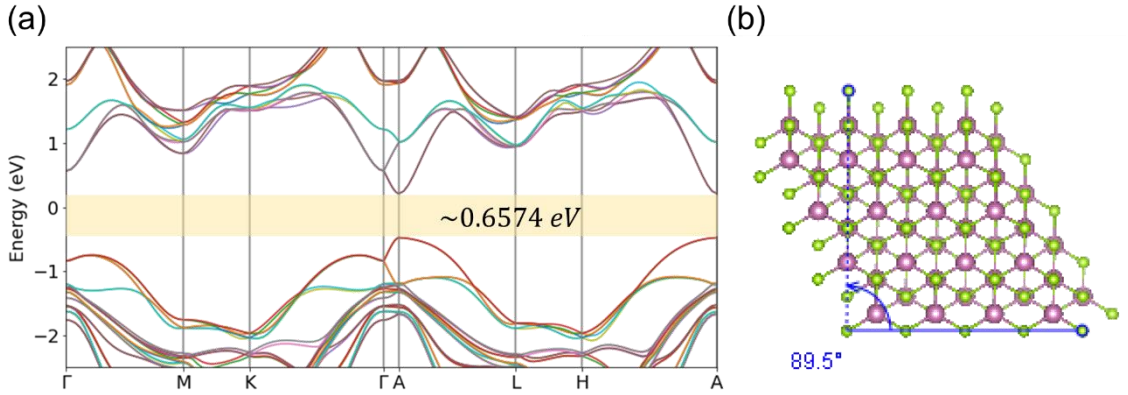

Fig 3-5 Band structure (a) and crystal structure (b) of InSe with -1% strain. The green atoms are Se and purple atoms are In.

doi:10.6342/NTU202301960

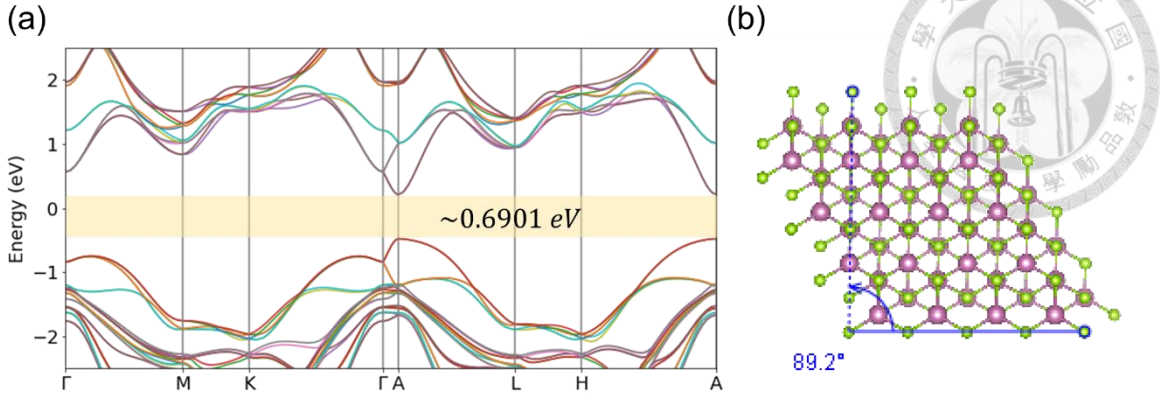

Fig 3-6 Band structure (a) and crystal structure (b) of InSe with -1.5% strain. The green atoms are Se and purple atoms are In.

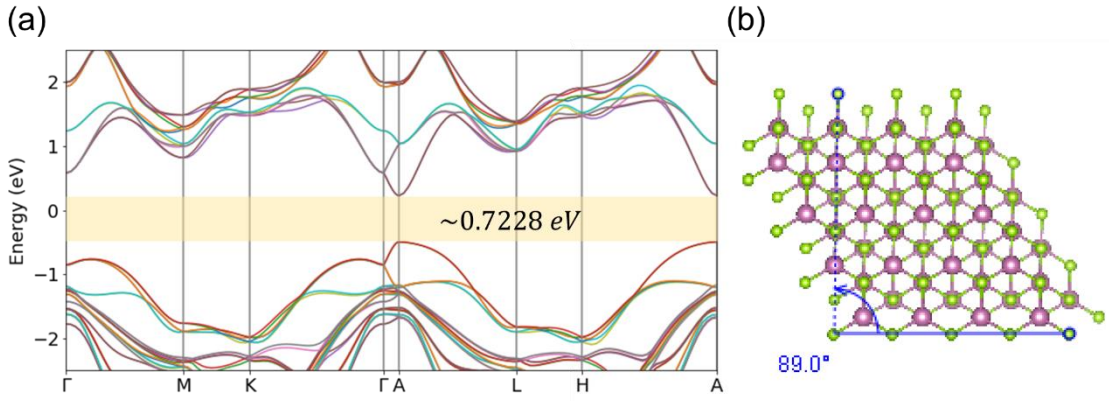

Fig 3-7 Band structure (a) and crystal structure (b) of InSe with -2% strain. The green atoms are Se and purple atoms are In.

3.2.2 Second-order Susceptibility Spectrum under Different Strain

The band gap of the unstrained InSe, as calculated through DFT in Fig 3-3, is approximately 0.5913 eV. This value is significantly lower than the band gap value (~1.2 eV) reported in existing literature [35] [36]. It is important to note that DFT calculations often underestimate band gap values, which may account for the discrepancy between the

doi:10.6342/NTU202301960

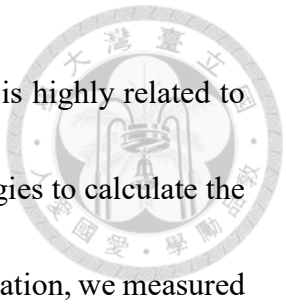

calculated and measured values in this case. However, the band gap is highly related to the second-order susceptibility and it's required to use real band energies to calculate the second-order susceptibility. To make the band gap close to the real situation, we measured the photoluminescence of our sample which peak position is around 1.24 eV (see section 4.2). Therefore, the scissor operation with 0.6487 eV was performed to increase the band gap in different strain cases. The calculated non-zero second-order susceptibility components of γ-InSe with different strain cases are displayed from Fig 3-8 to Fig 3-10. The x-axis of each figures represents the incident photon energy.

doi:10.6342/NTU202301960

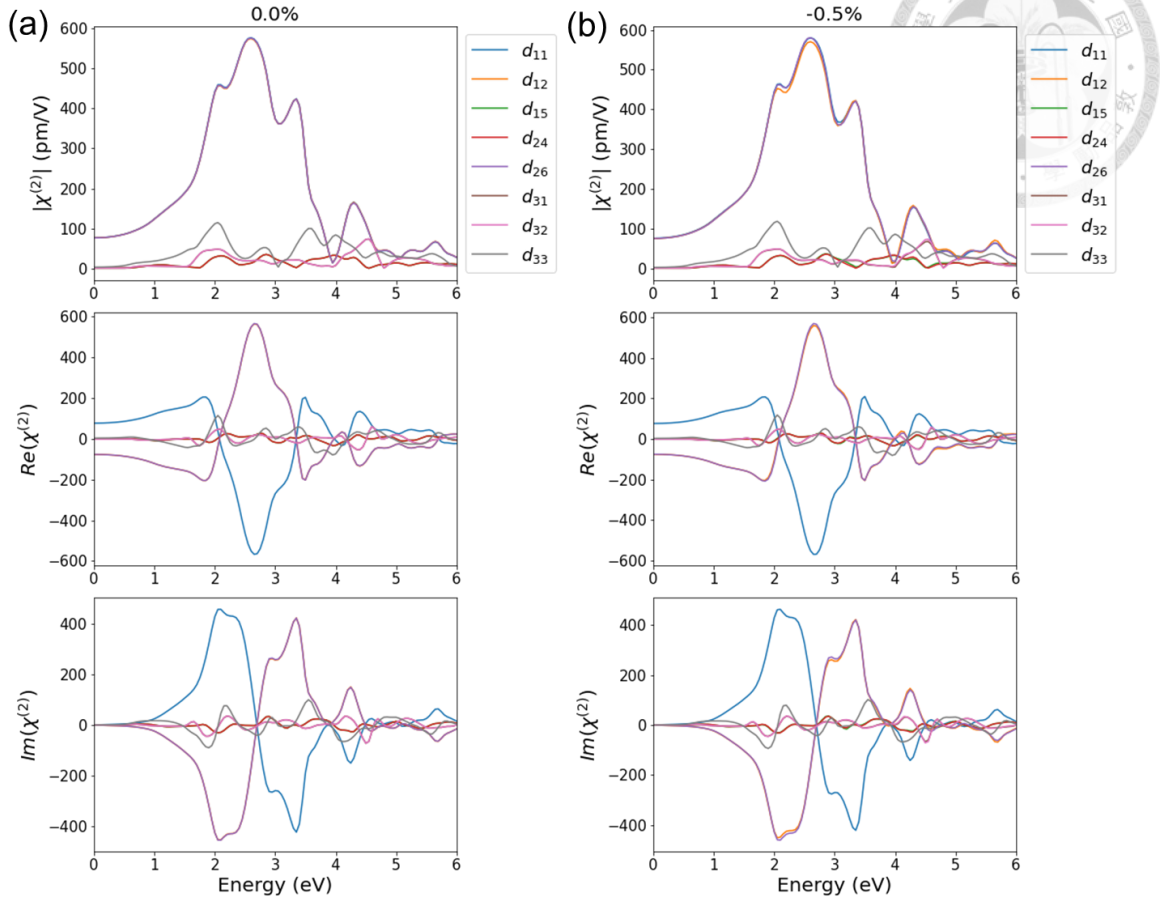

Fig 3-8 Computed the SHG susceptibility components of γ-InSe while subjecting it to strain levels of (a) 0% and (b) -0.5%.

doi:10.6342/NTU202301960

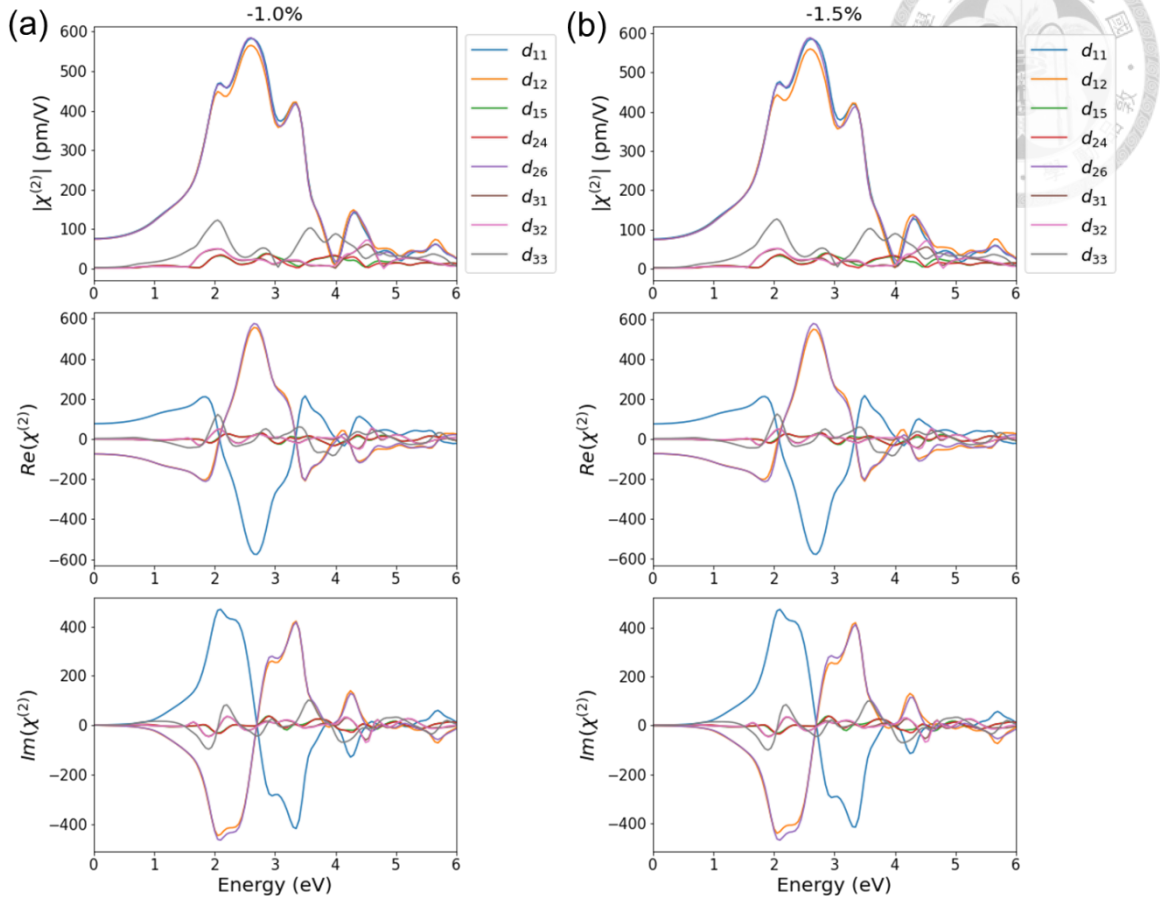

Fig 3-9 Computed the SHG susceptibility components of γ-InSe while subjecting it to strain levels of (a) -1% and (b) -1.5%.

doi:10.6342/NTU202301960

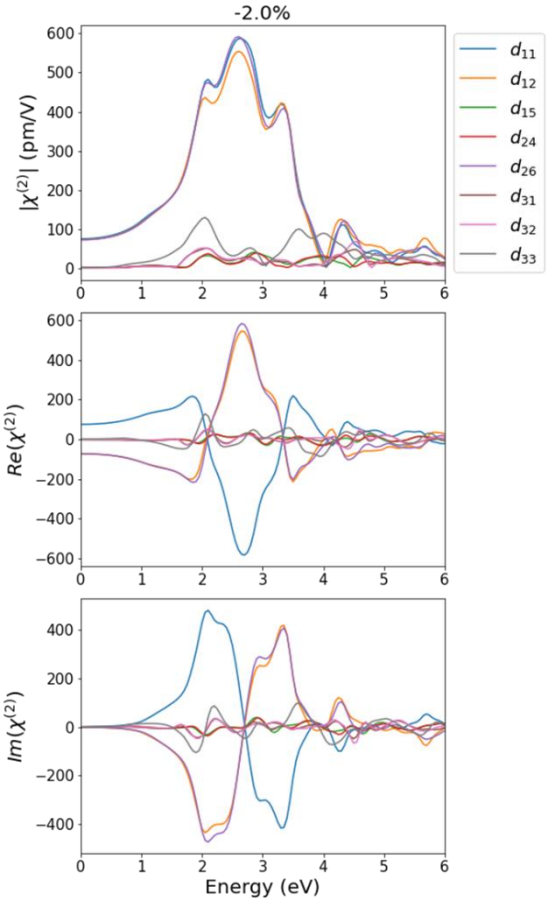

Fig 3-10 Computed the SHG susceptibility components of γ-InSe while subjecting it to strain levels of -2%

3.2.3 Angle-Resolved Second Harmonic Generation (SHG) under Different Strain

To determine the strain dependence, we analyze the susceptibility components at an incident photon energy of approximately 1.55 eV, which closely matches the experimental conditions. As the strain dependence experiment was conducted under normal incident conditions, we have only presented the component without the z-direction. The strain dependence diagrams are shown in Fig 3-11(a) and (b).

doi:10.6342/NTU202301960

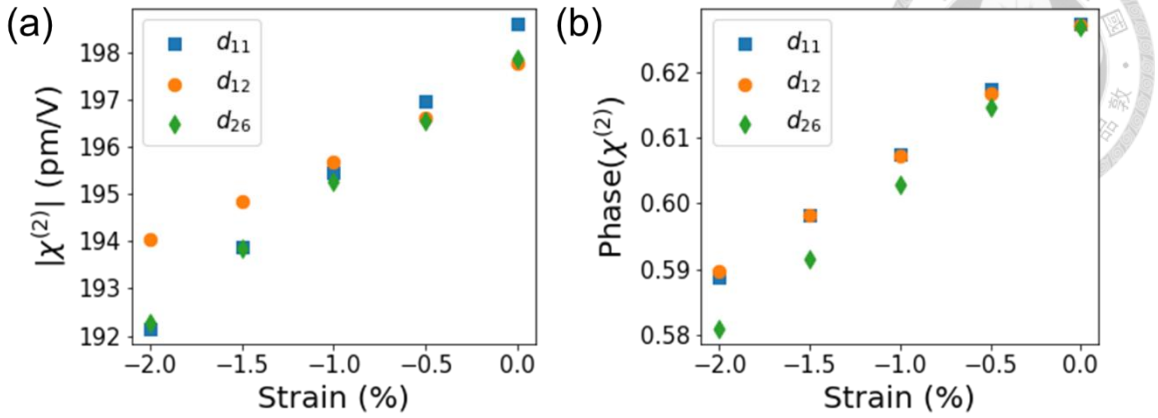

Fig 3-11 (a) Strain dependence diagram of absolute value of calculated second-order susceptibility components at 1.55 eV. (b) Strain dependence diagram of phase of calculated second-order susceptibility components at 1.55 eV.

Fig 3-11 (a) shows the linear relationship between second-order susceptibility components and strain. Based on the linear relationship, the second-order susceptibility with strain effect can be written as

$$d_{11}^{strain} = d_{11}^{0\%\,strain} + S\varepsilon, \qquad (3.19)$$

$$d_{12}^{strain} = d_{12}^{0\%\,strain} + L\varepsilon, \qquad (3.20)$$

$$d_{26}^{strain} = d_{26}^{0\%\,strain} + M\varepsilon, \qquad (3.21)$$

where S, L and M are the slopes, which can be obtained by fitting the data from first-principles calculation, and ε is strain. Note that $d_{11}^{0\%\,strain} = -d_{12}^{0\%\,strain} = -d_{26}^{0\%\,strain}$. By substituting modified second-order susceptibilities into equation (3.4),

doi:10.6342/NTU202301960

we can obtain the second-order polarization and do further calculation to get the intensity of SHG. The parallel SHG intensity ($I_{\parallel}^{(2\omega)}$) in terms of angle and strain is

$$I_{\parallel}^{(2\omega)} \propto \left| d_{11}^{0\%\ strain} \cos 3\theta + \varepsilon[S\cos^3\theta + (L+2M)\sin^2\theta\cos\theta] \right|^2. \qquad (3.22)$$

Equation (3.22) can be related to the unstrained case through its first term, which is obtained as equation (3.9). The effect of strain appears in the second term in equation (3.22) which is anisotropic feature. Fig 3-12 (a) and (b) display the parallel SHG intensity with -2% and -20% strain and compare with the 0% case. The polar plots clearly indicate that in cases of small strain, such as -2%, the SHG intensity decreases in a homogeneous manner. As the strain increases, it becomes apparent that the strain direction aligns with the x-axis ($0° - 180°$) due to the second term in equation (3.22).

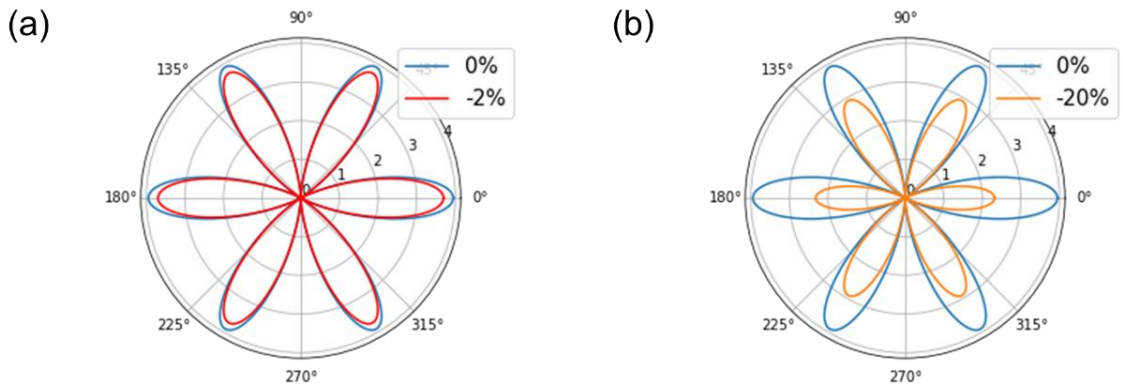

Fig 3-12 (a) Angle-resolved parallel SHG intensity polar plot by calculated $\chi^{(2)}$ at 1.55 eV under 0% and -2% strain. (b) Angle-resolved parallel SHG intensity polar plot by calculated $\chi^{(2)}$ at 1.55 eV under 0% and -20% strain.

doi:10.6342/NTU202301960

Chapter 4 Experiment Results and Discussion

4.1 Results of Second Harmonic Generation Confirmation

This section will demonstrate the results of the three signal confirmation methods that were discussed in section 2.1, including checking the signal wavelength, power dependent measurement and angle-resolved SHG measurement.

To know the peak wavelength of the detected signal, we replaced PMT by a spectrometer to detect the spectrum of the signal. The spectrum is shown in Fig 4-1 (a) and the peak position is ~395 nm which is the half of the incident wavelength (~790 nm).

Fig 4-1 (b) is the result of power dependent measurement and was plotted in log-log scale. In this figure, the data points show the linear relationship with the slope ~2 which indicates the detected signal and the input power is quadratic relation.

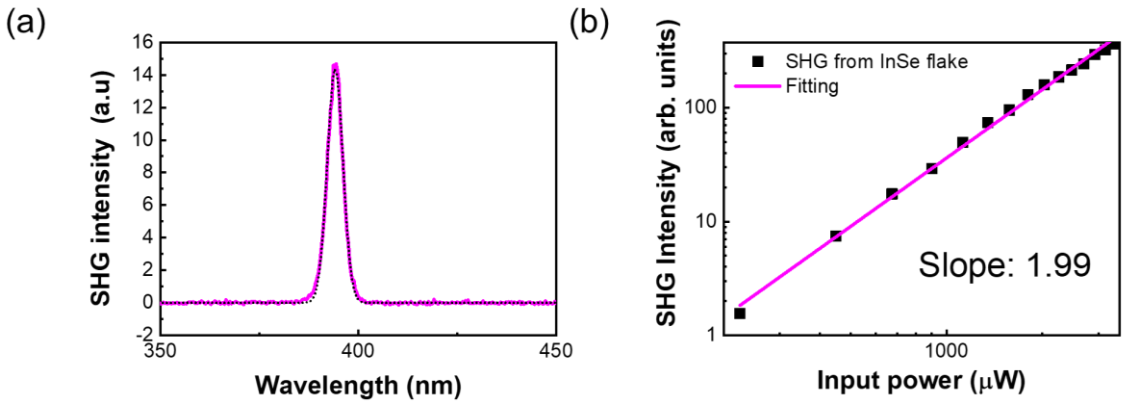

Fig 4-1 (a) Spectrum of the detected signal. The peak position is ~395 nm. (b) The power dependent diagram which plotted in log-log scale. The pink line is the linear fitting line

doi:10.6342/NTU202301960

of the data points (black square) and its slope is ~2.

The third method is to measure the angle-resolved SHG pattern. By means of the experimental setup described in Sec. 2.1, we measured the 400 nm signal in different rotational angle. Because of the imaging system in the experimental setup, the detected signal with specific polarization can be mapped on 2D image so as to easily observe the signal variation in different rotational angle. Fig 4-2 demonstrates the mapping images of the signal which polarization parallel to the incident laser.

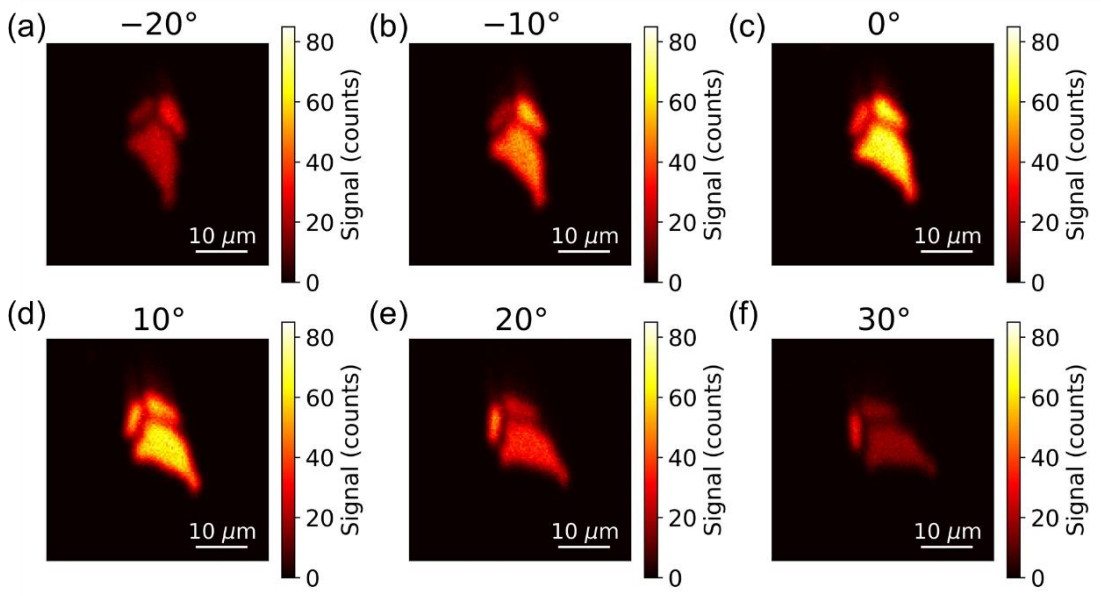

Fig 4-2 2D signal mapping images of the sample at angles ranging from −20° to 30° (a)-(f).

To quantitatively present the experimental results, we summed the photons in a

doi:10.6342/NTU202301960

region of the flake then plotted the angle-signal relationship in polar coordinates. Fig 4-3 shows the $I_{\parallel}$ and $I_{\perp}$ measurement results in polar coordinates which exhibit the six-fold symmetric patterns as Fig 3-1 (a) and (b)

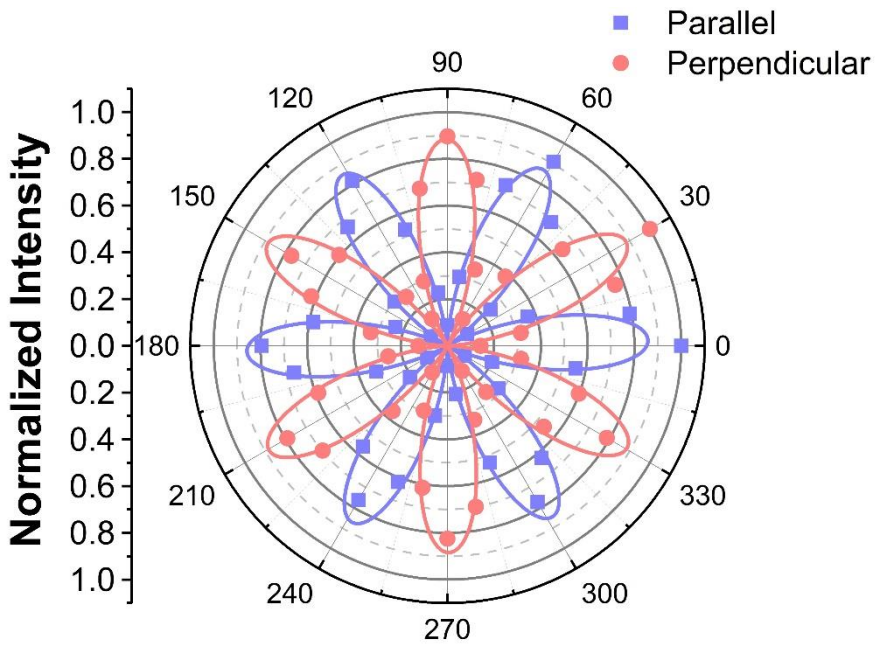

Fig 4-3 Polar plot of angle-resolved SHG with parallel intensity (blue) and perpendicular intensity (pink). The dots are experimental data and the lines are fitting curves.

The above experimental results provide the strong evidences to confirm the signal is second harmonic generation light from InSe.

4.2 Sample information

Raman spectroscopy is a powerful technique that can be used to identify the

doi:10.6342/NTU202301960

vibrational properties of a crystal. In the case of InSe, the crystal has a unique Raman spectrum that can be used to confirm its identity. Specifically, bulk InSe exhibits prominent Raman peaks at around 114 cm^{-1}, 175 cm^{-1} and 225 cm^{-1} [37]. To identify the crystal provided by Dr. Raman Sankar, we measured its Raman spectrum by the experiment setup referred in section 0. Fig 4-4 shows the result of the Raman spectrum. Since the measured peaks are around 114 cm^{-1}, 176 cm^{-1} and 227 cm^{-1}, which are very close to the reported values in the literature, the crystal was characterized to be InSe.

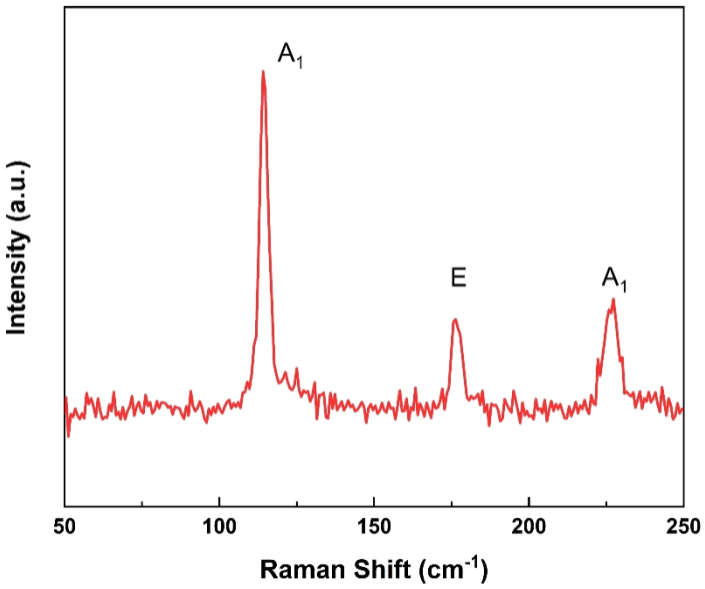

Fig 4-4 Raman spectrum of the crystal provided by Dr. Raman Shankar. The peaks of the modes are 114 cm^{-1}, 176 cm^{-1} and 227 cm^{-1}, which correspond to the vibrational modes of InSe (A_1, E, A_1).

InSe has direct bandgap in its bulk form and its band energy is about 1.2 eV in the

doi:10.6342/NTU202301960

reported literature. However, the calculated bandgap was lower than the what was reported (see section 3.2). To accurately determine the bandgap of the crystal and modify the calculated band structure through a scissor operation, we conducted PL measurements using the same equipment as the Raman measurements. The resulting spectrum is shown in Fig 4-5 and the peak position is around 1000 nm (~1.24 eV).

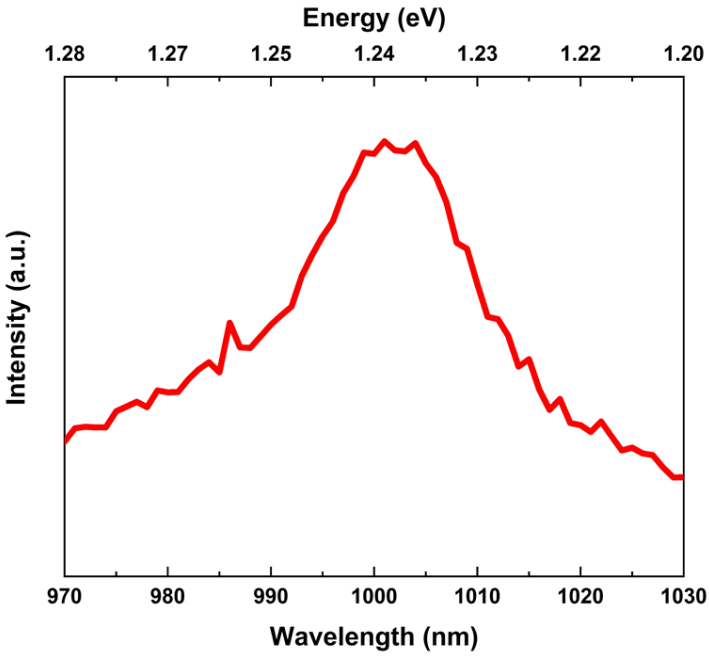

Fig 4-5 PL spectrum of the studied InSe crystal.

Even though the Raman spectrum and the PL measurement provide the evidence to confirm the crystal is InSe, the phase of the crystal still remain unknow since the ε and γ-phase exhibit the similar Raman modes and energy band gap [8] [38]. Therefore, we conducted the oblique incident SHG measurement to identify the phase of the InSe crystal

doi:10.6342/NTU202301960

by using the experimental setup referred in Sec. 2.2. As the discussion in section 3.1.3, Pin-Pout configuration was measured to investigate the stacking sequence, and the resulting data is presented in Fig 4-6. The similarity in the geometry of the patterns exhibiting 3-fold symmetry in Fig 4-6 and Fig 3-2 (a) provides evidence that the crystal is in the γ-phase.

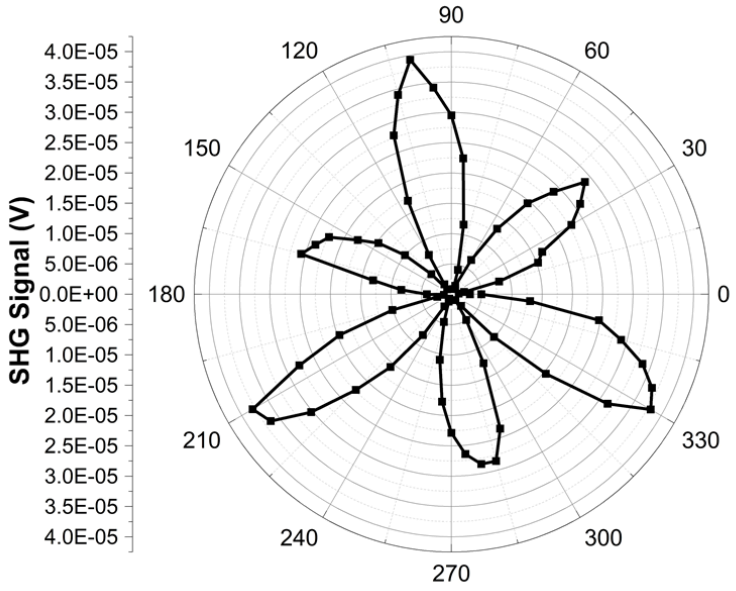

Fig 4-6 Pin-Pout configuration for angle-resolved SHG pattern.

In addition to characterizing the crystal phase, the thickness of the target sample was determined by using atomic force microscope (AFM). Note that the thickness of monolayer InSe is approximately 0.8 nm. [39] The AFM results is shown in Fig 4-7 and indicate the thickness of the sample is approximately 10 layers.

doi:10.6342/NTU202301960

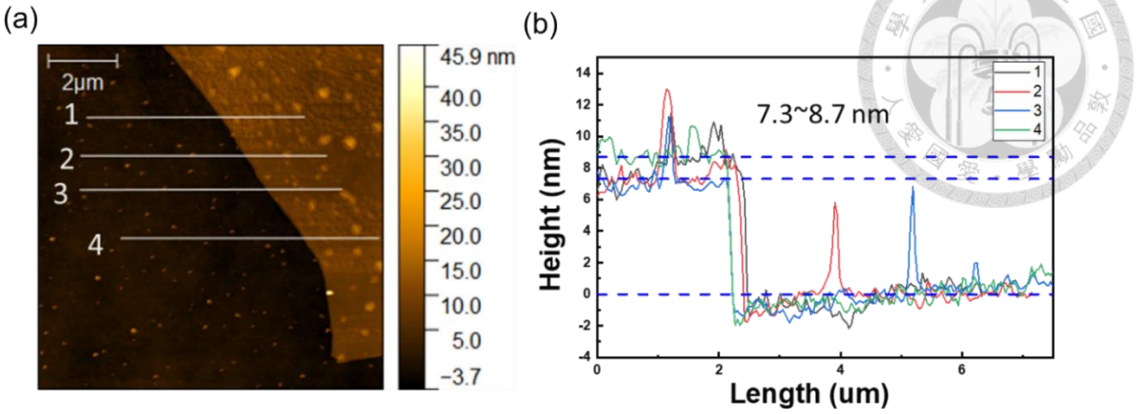

Fig 4-7 AFM measurement result of target sample thickness. (a) AFM image of the edge of the target sample. (b) The four labelled line profiles corresponding to (a) indicated that the sample thickness is approximately 8 nm or 10 layers.

4.3 Strain Dependence on Second Harmonic Generation from Few-layers InSe

To study the influence of strain on the SHG signal, we compressed the sample uniaxially along AC direction and measured the angle-resolved SHG pattern in different strain levels. The experimental results of angle-resolved SHG patterns under different strain levels (-0.18%, -0.36%, -0.53% and -0.83%) are shown in Fig 4-8. The strain direction in Fig 4-8 is along $0°$ to $180°$. The SHG intensity decrease as the strain level increase.

doi:10.6342/NTU202301960

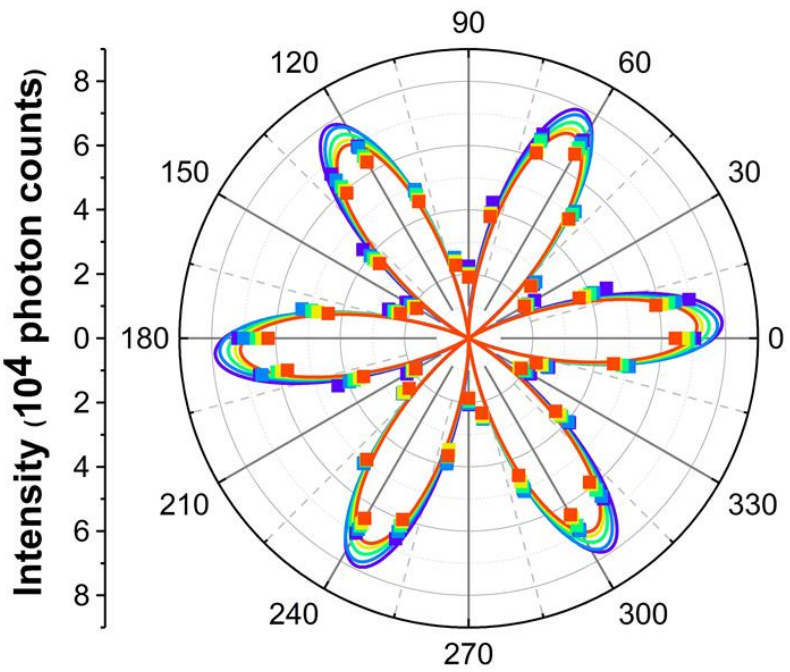

Fig 4-8 Angle-resolved SHG of few-layers InSe observed under varying levels of strain. The dots are the experimental data and the lines are fitting curve with $\cos^2 3\theta$ to be the guidance.

4.4 Discussion between First-Principles Results and Experimental Results

To check the appropriateness of the equation (3.22) based on the linear relationship observed from the results of first-principles calculation, we calculated the angle-resolved SHG with parallel intensity by equation (3.22) with the strain ε obtained from the experiments and fit it with the experiment data. A fitting parameter f^2 is multiplied on the right-hand side of equation (3.22) to be the scaling factor and the other parameters

doi:10.6342/NTU202301960

d_{11}, S, L and M are obtained from the first-principles results. The fitting results of 0% and -0.83% are shown in Fig 4-9 with the same scaling factor f^2. In Fig 4-9, it illustrates that while both experimental and theoretical data experience a decrease in intensity due to strain, the experimental data exhibits a greater drop.

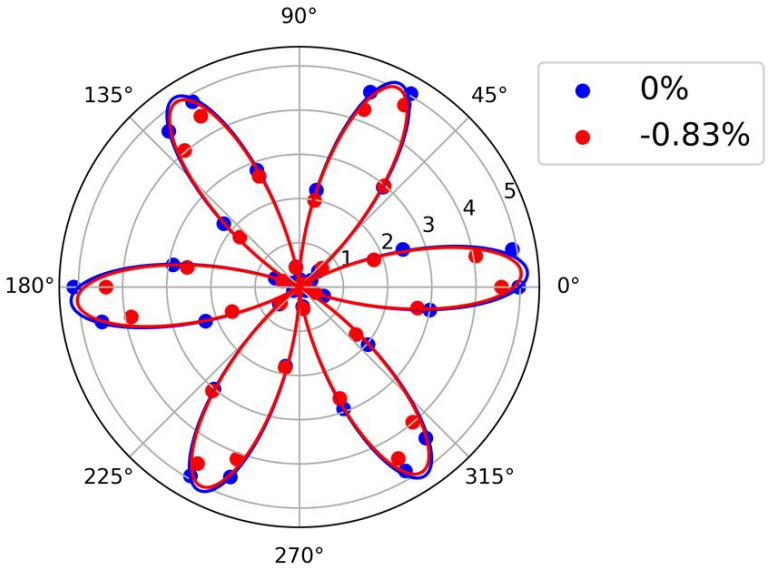

Fig 4-9 Fitting results based on the first-principles calculation and scaling factor f^2. The dots are experiment data and the solid lines are the fitting curves.

To quantitatively understand the differences between the experiment data and theoretical results, the coefficient of determination (r-squared values) were calculated for strain of -0.18%, -0.36%, -0.53% and -0.83%. The resulting values were 0.992, 0.987, 0.985, and 0.968, respectively, and shown in Fig 4-10. The r-squared value decreases while the strain level increases, which indicates the theoretical curves exhibit a greater

doi:10.6342/NTU202301960

deviation from the experimental results at higher strain.

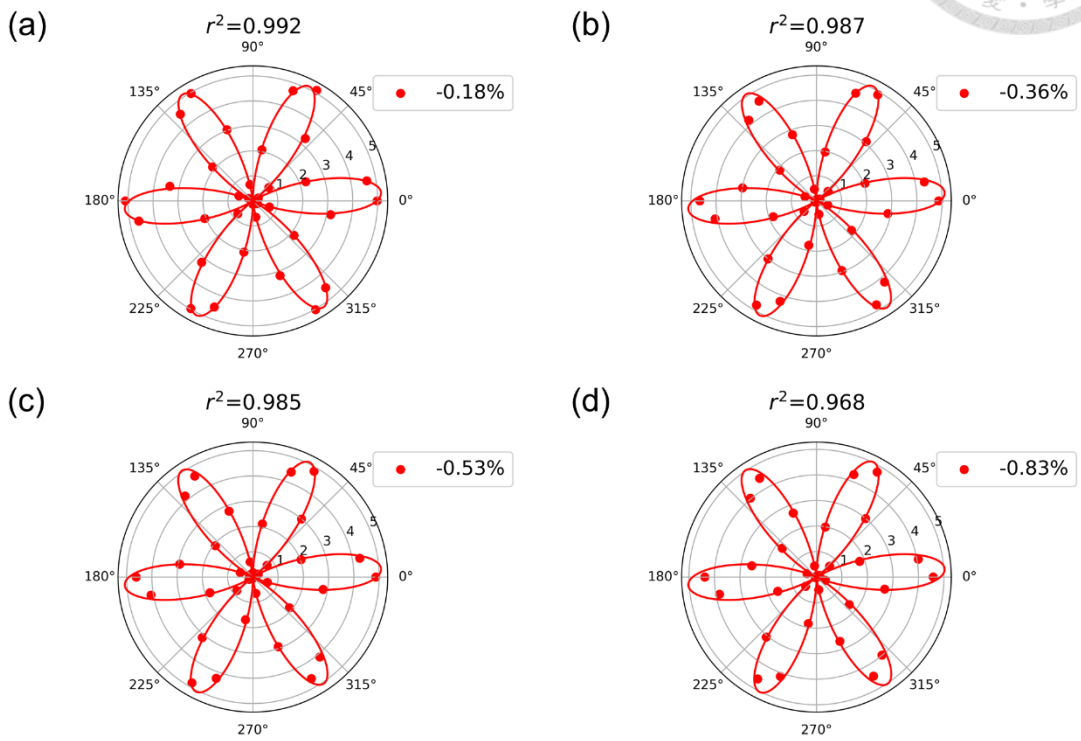

Fig 4-10 The fitting curves based on the first-principles results and the experiment data points with the r-squared values in each strain case.

It is necessary to modify the model in order to accurately fit the experimental data. Therefore, we multiplied the correction term f_2 before the strain term in equation (3.22) and the modified equation become

$$I_{\parallel}^{(2\omega)} = f^2\left|d_{11}^{0\%\,strain}\cos 3\theta + f_2\varepsilon[S\cos^3\theta + (L+2M)\sin^2\theta\cos\theta]\right|^2. \qquad (4.1)$$

The correction term f_2 was determined by maximizing the summation of the r-squared values in order to obtain the best fitting result. Fig 4-11 shows the fitting results with the

doi:10.6342/NTU202301960

correction term $f_2 = 4.48$ and the r-squared values of -0.18%, -0.36%, -0.53% and -0.83% strain cases were 0.993, 0.996, 0.996 and 0.995. The results indicate that the model relying solely on a correction parameter shows good quantitative agreement with experimental data when based on first-principles calculations.

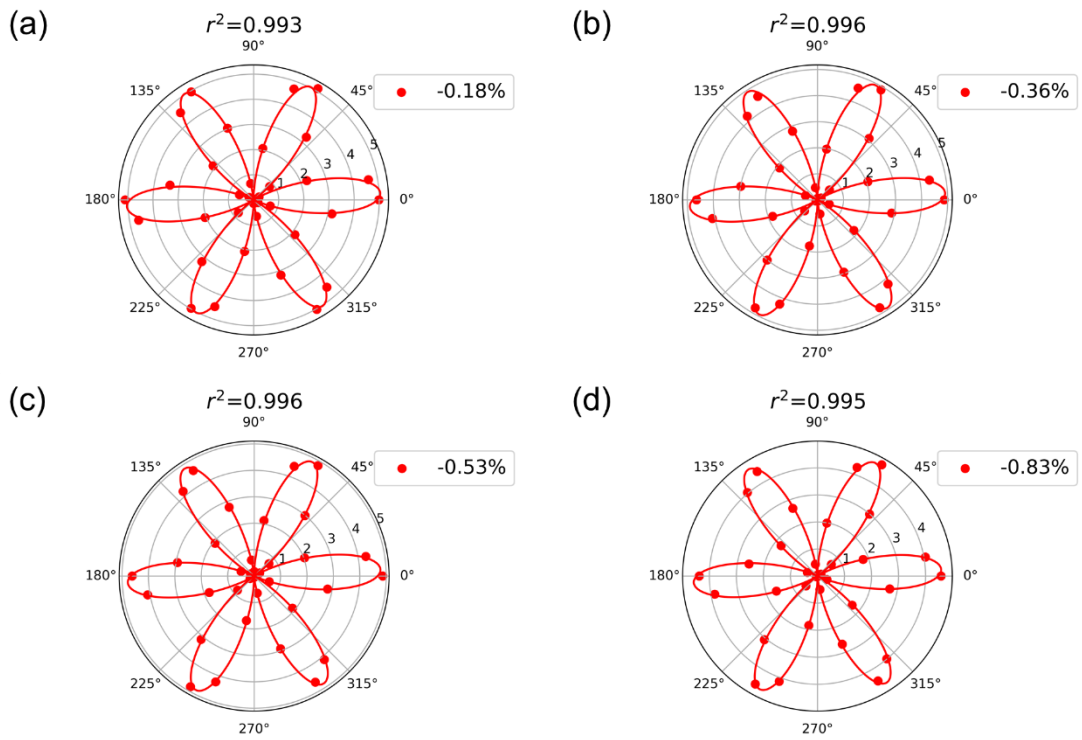

Fig 4-11 The fitting curves based on modified model and experiment data points with the r-squared values in each strain case.

doi:10.6342/NTU202301960

Chapter 5 Conclusion

In summary, we investigated the strain dependence on the angle-resolved SHG from γ-InSe by both experimental and theoretical approach.

In the experiment, the crystal was confirmed to be InSe by measuring its Raman spectrum. The energy band gap of the crystal was determined by the photoluminescence spectrum. We used the pulse laser to induce the double frequency light from the samples and confirmed the light was from second harmonic generation by different methods. For the phase confirmation, the oblique incident geometry was adopted to measure the angle-resolved SHG in Pin-Pout configuration and the result demonstrated the stacking mode belongs to the γ phase. The few-layers InSe flake was fabricated by the exfoliation method and its thickness was determined by atomic force microscopy. By considering the strain transfer efficiency, the substrate was chosen to be PEN with SU-8 on top, which is flexible and transparent. The sample was applied uniaxial strain by the self-design strain device. For the angle-resolved SHG measurement, we rotated the sample and mapped the SHG signal on 2D image in each rotational angle. The results of the experiment show that the intensity of the angle-resolved SHG decreases while the compressive strain level increases.

For the theoretical approach, we learned the mathematical description of angle-resolved second harmonic generation. We found that the structure related part is the

doi:10.6342/NTU202301960

second-order susceptibilities during the derivation. Therefore, we introduced the first-principles method to calculate the second-order susceptibilities under different strain cases. The calculation results show a linear relationship between the compressive strain and the second-order susceptibility at the incident photon energy in experimental condition. With the linear relationship, we modified the second-order susceptibilities and recalculate the angle-resolved SHG with parallel intensity. The results show the intensities drop in each angle, which is similar to the experimental results. In the case of large strain, such as -20% strain, it shows the 2-fold symmetry in the angle-resolved pattern, indicating the uniaxial strain direction.

Even though both the experimental and the theoretical results show the same behavior of the strain effect, there is still a difference as we fit the experimental data by the model based on the first-principles results. We quantified the difference by the r-squared values of the fitting results in each strain case. It shows that the r-squared value becomes lower with larger strain, which indicates the first-principles method underestimated the strain effect. When we added a correction term to modify the fitting model, the first-principles results agreed well with the experimental results.

doi:10.6342/NTU202301960

Reference

[1] Tamalampudi, S.R.; Lu, Y.-Y.; U, R.K.; Sankar, R.; Liao, C.-D.; Cheng, C.-H.; Chou, F.C.; Chen, Y.-T. *High performance and bendable few-layered InSe photodetectors with broad spectral response*. *Nano letters* **2014**, *14*, 2800-2806.

[2] Sucharitakul, S.; Goble, N.J.; Kumar, U.R.; Sankar, R.; Bogorad, Z.A.; Chou, F.-C.; Chen, Y.-T.; Gao, X.P. *Intrinsic electron mobility exceeding 10^3 $cm^2/(V\,s)$ in multilayer InSe FETs*. *Nano letters* **2015**, *15*, 3815-3819.

[3] Li, Y.; Wang, T.; Wu, M.; Cao, T.; Chen, Y.; Sankar, R.; Ulaganathan, R.K.; Chou, F.; Wetzel, C.; Xu, C.-Y. *Ultrasensitive tunability of the direct bandgap of 2D InSe flakes via strain engineering*. *2D Materials* **2018**, *5*, 021002.

[4] Leisgang, N.; Roch, J.G.; Froehlicher, G.; Hamer, M.; Terry, D.; Gorbachev, R.; Warburton, R.J. *Optical second harmonic generation in encapsulated single-layer InSe*. *AIP Advances* **2018**, *8*, 105120.

[5] Grimaldi, I.; Gerace, T.; Pipita, M.; Perrotta, I.; Ciuchi, F.; Berger, H.; Papagno, M.; Castriota, M.; Pacilé, D. *Structural investigation of InSe layered semiconductors*. *Solid State Communications* **2020**, *311*, 113855.

[6] Srour, J.; Badawi, M.; El Haj Hassan, F.; Postnikov, A. *Comparative study of structural and electronic properties of GaSe and InSe polytypes*. *The Journal of chemical physics* **2018**, *149*, 054106.

[7] Boukhvalov, D.W.; Gürbulak, B.; Duman, S.; Wang, L.; Politano, A.; Caputi, L.S.; Chiarello, G.; Cupolillo, A. *The advent of indium selenide: Synthesis, electronic properties, ambient stability and applications*. *Nanomaterials* **2017**, *7*, 372.

[8] Hao, Q.; Yi, H.; Su, H.; Wei, B.; Wang, Z.; Lao, Z.; Chai, Y.; Wang, Z.; Jin, C.; Dai, J. *Phase identification and strong second harmonic generation in pure ε-InSe and its alloys*. *Nano letters* **2019**, *19*, 2634-2640.

[9] Sun, Z.; Zhang, Y.; Qian, J.; Qiao, R.; Li, X.; Wang, Z.; Zheng, C.; Liu, K.; Cao, T.; Liu, W.T. *Compelling Evidence for the ε-Phase InSe Crystal by Oblique Incident Second Harmonic Generation*. *Advanced Optical Materials* **2022**, *10*, 2201183.

[10] Momma, K.; Izumi, F. *VESTA 3 for three-dimensional visualization of crystal, volumetric and morphology data*. *Journal of applied crystallography* **2011**, *44*, 1272-1276.

[11] Deckoff-Jones, S.; Zhang, J.; Petoukhoff, C.E.; Man, M.K.; Lei, S.; Vajtai, R.; Ajayan, P.M.; Talbayev, D.; Madéo, J.; Dani, K.M. *Observing the interplay between surface and bulk optical nonlinearities in thin van der Waals crystals*. *Scientific reports* **2016**, *6*, 22620.

doi:10.6342/NTU202301960

[12] Lee, J.-U.; Woo, S.; Park, J.; Park, H.C.; Son, Y.-W.; Cheong, H. *Strain-shear coupling in bilayer MoS2*. *Nature communications* **2017**, *8*, 1370.

[13] Mohiuddin, T.; Lombardo, A.; Nair, R.; Bonetti, A.; Savini, G.; Jalil, R.; Bonini, N.; Basko, D.; Galiotis, C.; Marzari, N. *Uniaxial strain in graphene by Raman spectroscopy: G peak splitting, Grüneisen parameters, and sample orientation*. *Physical Review B* **2009**, *79*, 205433.

[14] Mennel, L.; Furchi, M.M.; Wachter, S.; Paur, M.; Polyushkin, D.K.; Mueller, T. *Optical imaging of strain in two-dimensional crystals*. *Nature communications* **2018**, *9*, 1-6.

[15] Powers, P.E.; Haus, J.W. *Fundamentals of nonlinear optics*. CRC press: 2017.

[16] Boyd, R.W. *Nonlinear optics*. Academic press: 2020.

[17] Liang, J.; Zhang, J.; Li, Z.; Hong, H.; Wang, J.; Zhang, Z.; Zhou, X.; Qiao, R.; Xu, J.; Gao, P. *Monitoring local strain vector in atomic-layered $MoSe_2$ by second-harmonic generation*. *Nano letters* **2017**, *17*, 7539-7543.

[18] Kumar, N.; Najmaei, S.; Cui, Q.; Ceballos, F.; Ajayan, P.M.; Lou, J.; Zhao, H. *Second harmonic microscopy of monolayer MoS_2*. *Physical Review B* **2013**, *87*, 161403.

[19] Ribeiro-Soares, J.; Janisch, C.; Liu, Z.; Elías, A.; Dresselhaus, M.; Terrones, M.; Cançado, L.; Jorio, A. *Second harmonic generation in WSe_2*. *2D Materials* **2015**, *2*, 045015.

[20] Janisch, C.; Wang, Y.; Ma, D.; Mehta, N.; Elías, A.L.; Perea-López, N.; Terrones, M.; Crespi, V.; Liu, Z. *Extraordinary second harmonic generation in tungsten disulfide monolayers*. *Scientific reports* **2014**, *4*, 1-5.

[21] Li, Z.; Lv, Y.; Ren, L.; Li, J.; Kong, L.; Zeng, Y.; Tao, Q.; Wu, R.; Ma, H.; Zhao, B. *Efficient strain modulation of 2D materials via polymer encapsulation*. *Nature communications* **2020**, *11*, 1151.

[22] Liu, Z.; Amani, M.; Najmaei, S.; Xu, Q.; Zou, X.; Zhou, W.; Yu, T.; Qiu, C.; Birdwell, A.G.; Crowne, F.J. *Strain and structure heterogeneity in MoS_2 atomic layers grown by chemical vapour deposition*. *Nature communications* **2014**, *5*, 1-9.

[23] Mennel, L.; Paur, M.; Mueller, T. *Second harmonic generation in strained transition metal dichalcogenide monolayers: MoS_2, $MoSe_2$, WS_2, and WSe_2*. *APL Photonics* **2019**, *4*, 034404.

[24] Chung, S.; Park, S.; Technology. *Effects of temperature on mechanical properties of SU-8 photoresist material*. *Journal of Mechanical Science* **2013**, *27*, 2701-2707.

[25] Perdew, J.P.; Burke, K.; Ernzerhof, M. *Generalized gradient approximation made simple*. *Physical review letters* **1996**, *77*, 3865.

doi:10.6342/NTU202301960

[26] Morrison, I.; Bylander, D.; Kleinman, L. *Nonlocal Hermitian norm-conserving Vanderbilt pseudopotential*. *Physical Review B* **1993**, *47*, 6728.

[27] Ozaki, T. *Variationally optimized atomic orbitals for large-scale electronic structures*. *Physical Review B* **2003**, *67*, 155108.

[28] The code, OpenMX, pseudoatomic basis functions, and pseudopotentials are available on a website, http://www.openmx-square.org/.

[29] Onida, G.; Reining, L.; Rubio, A. *Electronic excitations: density-functional versus many-body Green's-function approaches*. *Reviews of modern physics* **2002**, *74*, 601.

[30] Ghahramani, E.; Moss, D.; Sipe, J. *Full-band-structure calculation of second-harmonic generation in odd-period strained $(Si)_n/(Ge)_n$ superlattices*. *Physical Review B* **1991**, *43*, 8990.

[31] Duan, C.-g.; Li, J.; Gu, Z.-q.; Wang, D.-s. *First-principles calculation of the second-harmonic-generation coefficients of borate crystals*. *Physical Review B* **1999**, *60*, 9435.

[32] Island, J.O.; Kuc, A.; Diependaal, E.H.; Bratschitsch, R.; Van Der Zant, H.S.; Heine, T.; Castellanos-Gomez, A. *Precise and reversible band gap tuning in single-layer $MoSe_2$ by uniaxial strain*. *Nanoscale* **2016**, *8*, 2589-2593.

[33] Lee, C.-C.; Lee, Y.-T.; Fukuda, M.; Ozaki, T. *Tight-binding calculations of optical matrix elements for conductivity using nonorthogonal atomic orbitals: Anomalous Hall conductivity in bcc Fe*. *Physical Review B* **2018**, *98*, 115115.

[34] Jatirian-Foltides, E.; Escobedo-Alatorre, J.; Márquez-Aguilar, P.; Hardhienata, H.; Hingerl, K.; Alejo-Molina, A. *About the calculation of the second-order susceptibility $\chi^{(2)}$ tensorial elements for crystals using group theory*. *Revista mexicana de física E* **2016**, *62*, 5-13.

[35] Wu, M.; Xie, Q.; Wu, Y.; Zheng, J.; Wang, W.; He, L.; Wu, X.; Lv, B. *Crystal structure and optical performance in bulk γ-InSe single crystals*. *AIP Advances* **2019**, *9*, 025013.

[36] Brotons-Gisbert, M.; Andres-Penares, D.; Suh, J.; Hidalgo, F.; Abargues, R.; Rodriguez-Canto, P.J.; Segura, A.; Cros, A.; Tobias, G.; Canadell, E. *Nanotexturing to enhance photoluminescent response of atomically thin indium selenide with highly tunable band gap*. *Nano letters* **2016**, *16*, 3221-3229.

[37] Sánchez-Royo, J.F.; Muñoz-Matutano, G.; Brotons-Gisbert, M.; Martínez-Pastor, J.P.; Segura, A.; Cantarero, A.; Mata, R.; Canet-Ferrer, J.; Tobias, G.; Canadell, E. *Electronic structure, optical properties, and lattice dynamics in atomically thin indium selenide flakes*. *Nano Research* **2014**, *7*, 1556-1568.

[38] Wu, M.; Xie, Q.; Wu, Y.; Zheng, J.; Wang, W.; He, L.; Wu, X.; Lv, B. *Crystal structure and optical performance in bulk γ-InSe single crystals*. *AIP Advances*

doi:10.6342/NTU202301960

2019, *9*, 025013.

[39] Zhou, J.; Shi, J.; Zeng, Q.; Chen, Y.; Niu, L.; Liu, F.; Yu, T.; Suenaga, K.; Liu, X.; Lin, J. *InSe monolayer: synthesis, structure and ultra-high second-harmonic generation*. *2D Materials* **2018**, *5*, 025019.

doi:10.6342/NTU202301960